Application of Fluidic Control within a Plano-Convex Singlet Lens

Eric Gutierrez[1], Nickolaos Savidis[2], James Schwiegerling[2,3]

Dept. of Mechanical Engineering[1], University of California, Riverside, Riverside, CA 92521; College of Optical Sciences[2], Dept. of Ophthalmology & Vision Science[3], University of Arizona, Tucson, AZ 85721

Integrated Optics for Undergraduates *(IOU)*

An NSF-ERC sponsored Research Experience for Undergraduates (REU) Program

This paper focuses on designing a computer code for the purpose of developing a systematic method for continuous control of the focal length of a plano-convex fluidic lens and utilizing the code for studying the optical behavior of a plano-convex fluidic lens. A syringe, which was controlled by a syringe pump controller, was utilized for fluid control. The code decreased the operation time for the syringe pump controller by replacing the manual push of buttons with a few clicks on a computer. By utilizing the code, the focal length of the fluidic lens was measured as a function of the curvature of the lens' flexible membrane. This was accomplished for three lasers of differing wavelengths (red: 633 nm; green: 543 nm; blue: 488 nm). A graphical relationship was found for the three wavelengths: as the lens curvature increased, the focal length decreased. In addition, as expected, the longer wavelength outputted a longer focal length per lens curvature.

Keywords: fluidic lenses, focal length, wavelength, fluidic control

1. Introduction

Fluidic lenses are an emerging field in optics research. Unlike standard zoom lenses, which depend on mechanically moving optics to adjust focus (e.g. focal length), fluidic lenses offer the capability of changing focal lengths while eliminating the need to adjust lens position**.** Fluidic lenses offer a wide variety of applications, and fabrication techniques are almost limitless[1]. They can be utilized in applications, such as free-space optical communications, adaptive optics, corrective eyewear, and cell phone cameras. These optical devices allow designers in various fields new and innovative opportunities to improve the performance, accuracy, throughput, reliability and overall cost of their devices[1].

Fluidic lenses are based on a flexible membrane and fluidic pressure. A flexible membrane encloses a specific amount of fluid. The hydrostatic pressure is manipulated to control the curvature of the flexible membrane[2]. Hence, when the hydrostatic pressure in the liquid-filled lens cavity is altered, the curvature of the membrane surface morphs to either a concave or convex surface[3], altering the optical wavefront of light passing through the membrane. As a consequence, a variable focal length is achieved.

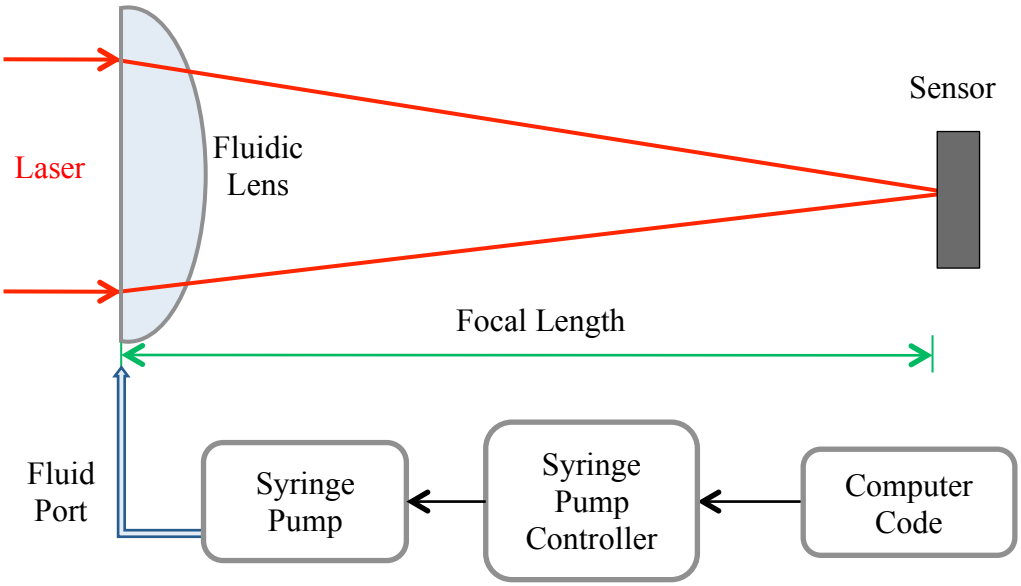

Figure 1. Schematic of the experimental setup.

2. Experimental Methods

The elastic membrane discussed was composed of polydimethylsiloxane (PDMS). We chose the PDMS as the membrane material due to its exceptional optical properties and elastic behavior. In addition, it is highly transparent in the range of visible light[4]. We made the PDMS in a clean room by pouring a mixture of PDMS and its curing agent on a glass mold. A vacuum was applied to remove air bubbles. The mixture was heated for a specific amount of time, removed from the mold, cured, and mounted into a holder.

The optical behavior of a fluidic lens was studied by varying the amount of deionized (DI) water housed inside the cavity of the lens. Adjusting the amount of fluid was accomplished by computationally manipulating a syringe pump controller with a MATLAB computer code. The syringe pump controller manipulated the axial displacement of a plunger located inside a cylindrical tube. The plunger and tube made up a 500 µL syringe. The amount of fluid infused or withdrawn from the lens cavity was influenced by pulling or pushing the plunger along the tube. This achieved both positive and negative power corrections with the lens. A fluid port, which transferred the DI water into and out of the fluidic lens, connected the syringe to the fluidic lens. Figure 1 illustrates the schematic of the experimental setup.

The focal length of the fluidic lens was measured as a function of the curvature of the membrane. The code was designed so that the position of the plunger in the tube corresponded to a specific curvature of the lens. The exterior of the glass tube consisted of markings from 0 to 500 µL. The code was constructed so that the syringe pump controlled the syringe by displacing the plunger in unit steps; moving the plunger one unit step translated to inputting or extracting 12.5 µL of DI water from the lens. Inputting a negative value withdrew fluid while a positive value infused fluid, which increased the lens'

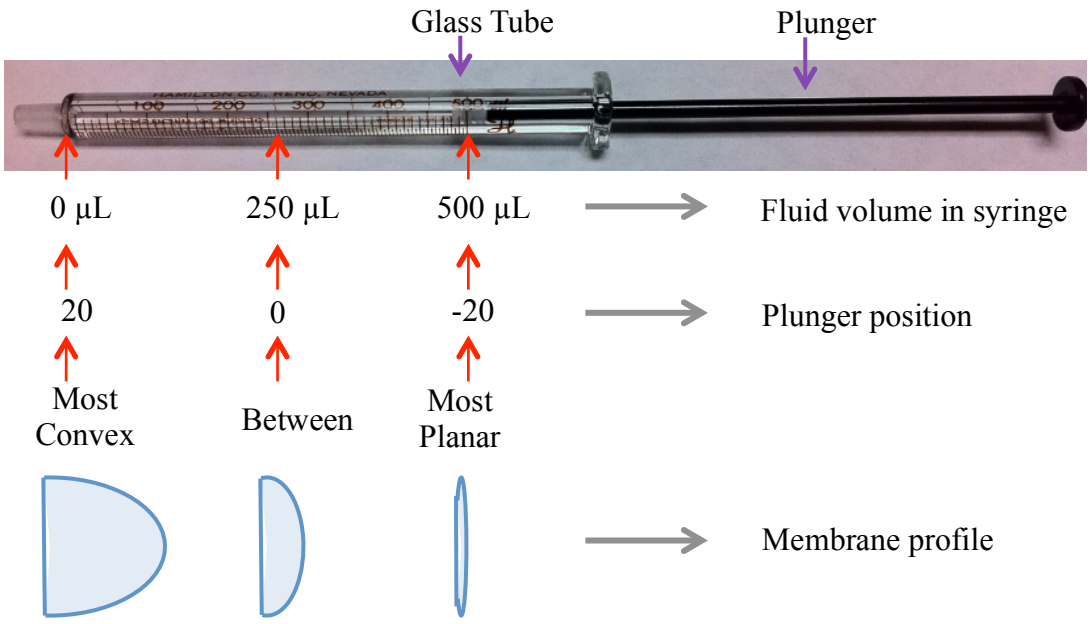

Figure 2. Plunger position relative to the amount of volume in the syringe (µL) and lens membrane profile. The plunger in the syringe shown is in the plunger position at -20.

curvature. The code was designed so that the user could input values from -20 to 20, allowing for the maximum value of 20 steps the plunger could shift relative to our zero point.

Our study samples focused on the cases where the lens surfaces were convex due to the replication of a plano-convex lens. The step position at -20 was where the lens was approximately planar; this correlated to the case where the plunger was at the 500 µL mark in the syringe tube. The step position at 20 was where the lens was at its most convex or 0 µL of fluid was left in the syringe. The case where the plunger was at the 0 step position, or zero point, was a convex surface between planar and most convex; this was also the marked center of the syringe where the plunger was placed at 250 µL. The three cases can be seen in Figure 2. This method, which allowed the continuous change in focal length of a fluidic lens, drastically decreased the time and effort to operate a syringe pump controller by replacing the manual push of buttons on the pump.

By utilizing this code, the graphical relationships between the focal length and the plunger position for different wavelengths were measured. Since varying the wavelength alters the focal length according to the optical properties of light, three lasers of different wavelengths (red: 633 nm; green: 543 nm; blue: 488 nm) were expanded and collimated through our testing apparatus. Forty-one separate focal lengths at forty-one curvatures were measured for each laser wavelength as the light passed through the fluidic lens. Because accuracy is of most importance, three trials were performed for each of the forty-one positions measured per wavelength and averaged to determine the best focal length.

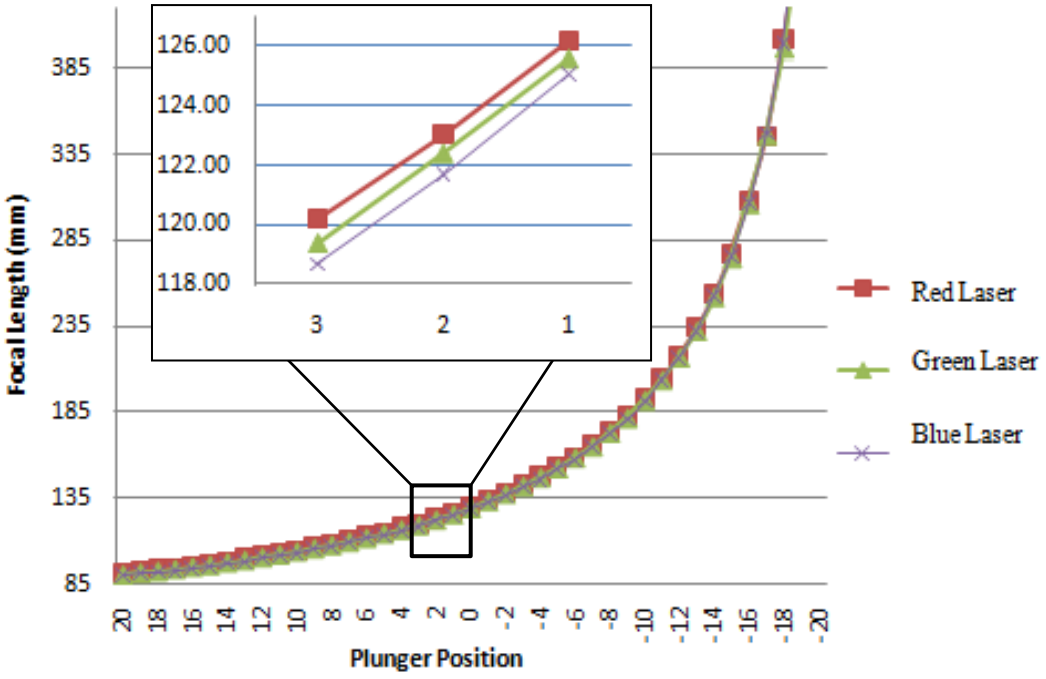

Figure 3. Focal length versus the plunger position for the three different laser wavelengths (red: 633 nm; green: 543 nm; blue: 488 nm).

3. Results and Discussion

Figure 3 illustrates the focal length, mm, versus plunger position in the syringe for the three different emitting wavelengths. There are a total of 123 data points in the plot, with 41 points for each laser. Each of the 41 points is an averaged value of three trials. The separate graph for plunger positions at steps 1, 2, and 3 demonstrate the relationship between the three laser wavelengths.

As previously discussed, the plunger position at 20 corresponds to a convex lens, whereas the position at -20 corresponds to a planar lens. As fluid is extracted from the lens, or as the lens becomes less convex, the focal length increases. In the negative region, this relationship is much more drastic. On the other hand, as we shift to positive plunger positions, or when the lens becomes more convex, the change in focal length is less drastic. This phenomenon produces a relatively linear change in focal length with higher amounts of fluid in the lens chamber. The opposite occurs in the negative plunger position values; if the lens is close to planar, the change in focal length drastically increases. This non-linear curve correlates to the shape of the membrane; as the lens curvature becomes planar, the equal amount of fluid extraction offers greater variation in focal position.

Figure 3 also shows that the accuracy of our designed system allows for the distinction of wavelength focal position related to dispersion. Matching to dispersion theory, the focal length of the red wavelength is longer than the focal length of the green wavelength, which in turn is longer than the blue wavelength focal position. At any plunger

position, or at any curvature of the lens, the red laser will always have the furthest focal length relative to the shorter wavelength. Hence, as the wavelength increases, the focal length increases, and vice versa. Because refraction is wavelength-dependent within the same material, such as DI water, the fluid's dispersion is a significant factor in analysis and fluid selection within plano-convex fluidic lenses.

4. Conclusion

In this project we focused on designing a computer code for controlling the focal length of a plano-convex fluidic lens and utilizing the code for studying the optical properties of the lens. Our method for controlling the change in focal length of the fluidic lens drastically increased efficiency in analysis. The results showed the correlation between linear extraction of fluid volume and nonlinear focal positions. In addition, the measured results confirmed the significance of fluid selection due to wavelength dependent dispersions.

Acknowledgements

The authors would like to acknowledge support from the National Science Foundation through an REU Site under grant #EEC-1004331, as well as the University of Arizona, College of Optical Sciences for being the host of this project.

References

1. S. P. Casey, "Liquid Lens: Advances in Adaptive Optics," (paper presented at the Asia Communications and Photonics Conference and Exhibition, Shanghai, China, November 2, 2009), <http://www.opticsinfobase.org/abstract.cfm?URI=ACP-2009-FE3>.
2. R. Marks, D.L. Mathine, G. Peyman, J. Schwiegerling, N. Peyghambarian, "Adjustable Adaptive Compact Fluidic Phoropter With No Mechanical Translation of Lenses," *Optics Letters* 35, no. 5 (2010): 739-741.
3. W. Zhang, P. Liu, X. Wei, S. Zhuang, B. Yang, "The Analysis of the Wave Front Aberration Caused by the Gravity of the Tunable-Focus Liquid-Filled Membrane Lens," *Proceedings of the SPIE* 7849 (2010): 78491W, accessed June, 13, 2011, doi: 10.1117/12.869866.
4. H. Ren, D. Fox, P.A. Anderson, B. Wu, S.T. Wu, "Tunable-Focus Liquid Lens Controlled Using a Servo Motor," *Optics Express* 14, no. 18 (2006): 8031-8036, accessed June, 13, 2011, doi: 10.1364/OE.14.008031.

Transient Antihydrogen Production in a Paul Trap

G. Geyer and R. Blümel
Department of Physics, Wesleyan University, Middletown, Connecticut 06459-0155
(Dated: May 14, 2012)

Although positrons and antiprotons have vastly different masses, we show that it is possible to store both particle species simultaneously in a Paul trap, using the space charge of the positron cloud as a trap for the antiprotons. Computer simulations confirm the validity of this new trapping mechanism. In addition, the simulations show transient antihydrogen production that manifests itself in the intermittent production of bound positron-antiproton Rydberg states. Since realistic trapping parameters are used in the simulations, (i) simultaneous positron-antiproton trapping and (ii) transient antihydrogen formation should be experimentally observable in a Paul trap. Strategies are suggested to lengthen the lifetime of antihydrogen in the Paul trap.

PACS numbers: 37.10.Ty

I. INTRODUCTION

Motivation for the production of antihydrogen ($\bar{\mathrm{H}}$) is drawn from the following three main goals:

1. Spectroscopy of its energy levels to confirm the hypothesis that antihydrogen has the same spectrum as hydrogen.

2. Testing the effects of a gravitational field on antimatter.

3. Serving as a first step towards the storage of antimatter for efficient rocket propulsion.

The first item above constitutes a rigorous test of the Charge Conjugation-Parity-Time Reversal (CPT) invariance theorem [1], a fundamental element of the standard model of particle physics. The CPT theorem predicts that the spectra of atoms and anti-atoms should be exactly the same. Any difference in measured spectra of atoms and anti-atoms would be inconsistent with CPT invariance and would necessitate major revisions of the standard model.

The second item also has exciting implications for fundamental physics, since the weight of antimatter, i.e. the force it experiences in a gravitational field, has not yet been experimentally determined. Not even the sign of the gravitational force of antimatter is known. Although some authors argue that it should be the same as ordinary matter (see, e.g., [2, 3]), others argue that matter and antimatter should repel each other (see, e.g., [4]). Only direct experimentation on anti-atoms can resolve the dispute on the behavior of antimatter in a gravitational field. Indeed, within the framework of the AEGIS collaboration [5], e.g., such experiments are currently under way.

Regarding the third item, the simple structure of $\bar{\mathrm{H}}$ makes it one of the easier forms of antimatter to synthesize. Additionally, since it is electrically neutral, it takes relatively little input energy to bring antihydrogen into close proximity with hydrogen, which would be required in any efficient propulsion system. Since the ease of synthesis and efficient extraction of stored energy are essential to both the viability and the cost of a material as fuel, these are important concerns from an engineering perspective. This confluence of properties makes $\bar{\mathrm{H}}$ the most promising fuel source for a "perfect" matter-antimatter burning interstellar space ship [6].

In light of the discussed scientific and engineering impact that positive results on antimatter formation would have, many groups have been engaged in research regarding the production of $\bar{\mathrm{H}}$ for a number of years. The ALPHA [7, 8] and ATRAP [9, 10] collaborations have both been successful at detecting $\bar{\mathrm{H}}$ formation in different types of modified Penning traps. [7–10] After successfully trapping $\bar{\mathrm{H}}$ for 1000 s [11], the ALPHA collaboration has also demonstrated resonant quantum transitions in $\bar{\mathrm{H}}$ [8]. Magnetic traps, however, may not be optimal for the efficient formation of antimatter. Due to the Lorentz force, the magnetic fields impede the formation of neutral antimatter. In this paper, we investigate antimatter formation in an alternate trap that uses only electric fields: the Paul trap.

II. THEORETICAL BACKGROUND

A. Paul Trap Potential

The Paul trap [12] is a dynamical, charged-particle trap that consists of three conducting, axially symmetric, hyperbolic surfaces. A two-dimensional x-z cross section of the Paul-trap electrodes is sketched in Fig. 1. As shown, two of the electrodes intersect the x-z plane to form the two end-cap electrodes of the trap, while the third electrode forms the "ring electrode." The entire trap is axially symmetric about the z-axis.

As shown in Fig. 1, a superposition of a static (DC) voltage, U_0, and an alternating (AC) voltage with amplitude V_0 and frequency ω,

$$V(t) = U_0 + V_0 \cos(\omega t), \tag{1}$$

is applied between the ring electrode and the electrically connected end caps. The shape of the electrodes and

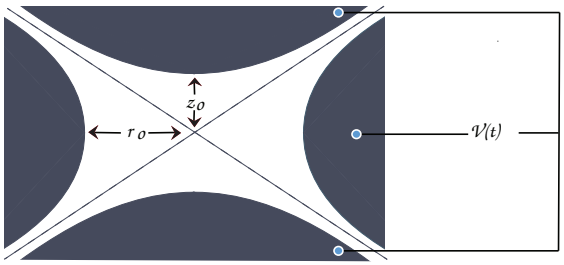

FIG. 1. Shown is a two-dimensional cross section (axially symmetric about the z-axis) of the three conducting surfaces (solid electrodes) that form the Paul trap [12]: the two end caps and the ring electrode. The cross section of the two end caps are represented by the two dark, hyperbolic sheets at the top and the bottom of the figure. The cross section of the ring electrode is represented by the two dark, hyperbolic regions at the left and the right of the figure. (The cross sections are drawn as solid areas rather than outlined because these electrodes are frequently "filled in" hyperboloids, i.e. machined from solid metal rather than formed from thin sheet metal.) The distance of the end-cap electrodes from the center of the trap is z_0; the distance of the ring-electrode from the center of the trap is r_0.

their arrangement is chosen such that the applied AC voltage creates an effective potential minimum, located at the center of the trap. It is this minimum which is capable of trapping charged particles forever.

For the following derivations, we note that the frequency of the AC voltage (typically ranging from a few MHz to about a GHz) and the amplitude of the AC voltage (typically on the order of a few hundred V or less) are small enough so that we can neglect magnetic field effects. This follows the usual computational treatment of the Paul trap in the literature (see, e.g., [12–14]), where magnetic fields are not considered.

If we define cylindrical coordinates in the usual way, with the z axis along the axis of symmetry of the trap and the x and y axes defined accordingly, and if we define $r^2 = x^2 + y^2$, the axial symmetry of the trap results in a potential of the form:

$$\Phi(x, y, z; t) = A(t)r^2 + B(t)z^2 \ . \tag{2}$$

According to Maxwell's equations in free space,

$$\nabla^2\Phi(x, y, z; t) = 0. \tag{3}$$

Using (2) in (3) yields

$$B(t) = -2A(t). \tag{4}$$

Thus, we have

$$\Phi(x, y, z; t) = A(t)(r^2 - 2z^2), \tag{5}$$

i.e. the potential, (2), has a hyperbolic shape that would not trap charged particles if A and B were time-independent, static coefficients. This is a consequence of Earnshaw's theorem [15], which states that an electrostatic potential satisfying (3) cannot have a potential minimum. However, since the trapping potential, (2), is due to an *alternating* electric field, the Paul trap potential can have a dynamic minimum without violating Earnshaw's theorem [12].

Taking the time-dependence of the trap into account, we can set the potential of the end-caps and ring electrode to be $-\Phi_0(t)$ and $\Phi_0(t)$ respectively. We also define the distance from the center of the trap to the ring electrode to be r_0, and from the center to the polar end caps to be z_0 (see Fig. 1). Then, at the intersection point of the upper end-cap electrode with the z axis ($r = 0, z = z_0$), we have:

$$\begin{aligned} -\Phi_0(t) &= -2A(t)z_0^2 \\ \implies \quad A(t) &= \frac{\Phi_0(t)}{2z_0^2}. \end{aligned} \tag{6}$$

Similarly, at the point ($r = r_0, z = 0$) on the ring electrode, we have:

$$\begin{aligned} \Phi_0(t) &= A(t)r_0^2 \\ \implies \quad A(t) &= \frac{\Phi_0(t)}{r_0^2}. \end{aligned} \tag{7}$$

Requiring

$$r_0^2 = 2z_0^2, \tag{8}$$

equations (6) and (7) are consistent and the potential, (5), becomes:

$$\Phi(x, y, z; t) = \frac{\Phi_0(t)}{r_0^2}(r^2 - 2z^2). \tag{9}$$

Let us now compute the time dependence. Since the applied voltage, (1), is the potential difference between the end-cap electrodes and the ring electrode, we have:

$$\begin{aligned} \Phi_0(t) - (-\Phi_0(t)) &= U_0 + V_0\cos(\omega t) \\ \implies \quad \Phi_0(t) &= \frac{U_0 + V_0\cos(\omega t)}{2}. \end{aligned} \tag{10}$$

Thus, the full, time-dependent form of our desired potential is written:

$$\Phi(x, y, z; t) = \frac{U_0 + V_0\cos(\omega t)}{2r_0^2}(r^2 - 2z^2). \tag{11}$$

B. Charged Particles in a Paul Trap

Now that we have the trapping potential, we are ready to describe the motion of a trapped particle with mass m and charge Q within the trap. Denoting the position vector of the particle by $\mathbf{r} = (x, y, z)$, using Newton's second law, $\mathbf{F} = m\ddot{\mathbf{r}}$, together with the fact that the force on a particle with charge Q is given by

$$\mathbf{F} = Q\mathbf{E} = -Q\nabla\Phi(\mathbf{r}; t), \tag{12}$$

we obtain:

$$m\frac{d^2\mathbf{r}}{dt^2} = -Q\frac{U_0 + V_0\cos(\omega t)}{r_0^2}\begin{pmatrix} x \\ y \\ -2z \end{pmatrix}. \qquad (13)$$

We simplify this equation by defining the following dimensionless constants:

$$a = \frac{4QU_0}{m\omega^2 r_0^2}\,, \quad q = \frac{2QV_0}{m\omega^2 r_0^2}\,, \quad \text{and} \quad \tau = \frac{\omega t}{2}, \qquad (14)$$

where τ is the dimensionless time. The two other constants, a and q, act as control parameters: they determine the stability of the system. Only certain pairs (a, q) will produce stable, trapped solutions of (13). This is easier to see once we simplify the equations of motion into a set of three uncoupled equations that have the form of Mathieu's Equations [16]:

$$\frac{d^2\mathbf{r}}{d\tau^2} + [a + 2q\cos(2\tau)]\begin{pmatrix} x \\ y \\ -2z \end{pmatrix} = 0. \qquad (15)$$

These are the canonical equations used to describe the motion of a charged particle in a Paul trap [12]. A physical analogy for the motion of a particle satisfying this relation would be to consider a saddle-shaped plate on a spinning platform [12]. When the platform is not spinning, which is analogous to the voltage not alternating (but still applied), a small ball placed somewhere near the center (or anywhere else) will roll off the side. However, if the saddle is spinning at an appropriate angular speed, the ball will remain on the platform and undergo a confined motion with small "zig-zag" perturbations about some average trajectory. That small scale motion is called the micro-motion while the larger-scale, average motion is called the macro-motion [17]. In the classical picture, there is a direct analogy between this mechanical situation and charged particles in a Paul trap.

III. NUMERICAL SIMULATIONS

The Paul trap excels at trapping charged particles of a single species. However, in general, it is not as effective at simultaneously trapping particles of different species. Consider our case: positrons and antiprotons have an equal magnitude of charge, but differ in mass by a factor of roughly 1836. The (a, q) pair for each of these particles will be accordingly different, so they cannot both be *independently* confined in a specifically tuned Paul trap. However, due to the Coulomb force, this does not rule out the possibility of these two oppositely charged particles being *simultaneously* trapped. In other words, their motion is no longer determined by the Paul trap potential alone. As we will confirm below, this creates new possibilities for stable trapping. Our simulations demonstrate this new type of stability and allow us to determine the viability of $\bar{\mathrm{H}}$ production in a Paul trap. Since the particles simulated are in a highly excited, relatively hot cloud state, quantum effects are expected to be exceedingly small, so our simulations are entirely classical.

A. Coupled Equations of Motion

In order to simulate interacting particles in the trap, we add the Coulomb force to the single-particle equation (15). To obtain dimensionless equations that can be simulated on a computer, we introduce a convenient unit of length, $l_0 = 1\,\mu$m, and define the dimensionless Coulomb constant

$$\Gamma = \frac{e^2}{m\omega^2\pi\epsilon_0 l_0^3}. \qquad (16)$$

We consider a system of N positrons and N' antiprotons, and introduce (in units of l_0) the dimensionless position vectors $\mathbf{r}_i = (x_i, y_i, z_i)$ for positron number i, and $\mathbf{R}_k = (X_k, Y_k, Z_k)$ for antiproton number k. Then, the dimensionless equations of motion for positrons number $i = 1, \ldots, N$, are:

$$\frac{d^2\mathbf{r}_i}{d\tau^2} + [a + 2q\cos(2\tau)]\begin{pmatrix} x_i \\ y_i \\ -2z_i \end{pmatrix} = \Gamma\sum_{\substack{j=1 \\ j\neq i}}^{N}\frac{\mathbf{r}_i - \mathbf{r}_j}{|\mathbf{r}_i - \mathbf{r}_j|^3} - \Gamma\sum_{j'=1}^{N'}\frac{\mathbf{r}_i - \mathbf{R}_{j'}}{|\mathbf{r}_i - \mathbf{R}_{j'}|^3}, \qquad (17)$$

and for antiprotons number $k = 1, \ldots, N'$, are:

$$\frac{d^2\mathbf{R}_k}{d\tau^2} - \frac{1}{\rho}[a + 2q\cos(2\tau)]\begin{pmatrix} X_k \\ Y_k \\ -2Z_k \end{pmatrix} = \frac{\Gamma}{\rho}\sum_{\substack{j'=1 \\ j'\neq k}}^{N'}\frac{\mathbf{R}_k - \mathbf{R}_{j'}}{|\mathbf{R}_k - \mathbf{R}_{j'}|^3} - \frac{\Gamma}{\rho}\sum_{j=1}^{N}\frac{\mathbf{R}_k - \mathbf{r}_j}{|\mathbf{R}_k - \mathbf{r}_j|^3}, \qquad (18)$$

where $\rho = M/m$ is the ratio of the antiproton mass M and the positron mass m.

B. Trap and Initial Conditions

According to the theory of Mathieu equations, trapping is achieved for (a, q) pairs in *stability tongues* [16]. For our simulations, we chose $a = 0$ and $q = 0.1$. This pair corresponds to a parameter combination in the fundamental stability tongue [16], and may be realized by choosing $U_0 = 0\,\mathrm{V}$ and $V_0 = 100\,\mathrm{V}$. We also chose the size of the trap to be $r_0 = 5\,\mathrm{mm}$. All of the above choices are motivated by similar parameters for Paul traps typically used in the lab (see, e.g., [13]). For positrons ($Q = e$, where e is the elementary charge) and this choice of trap parameters, we obtain $\omega = 2\pi \times 597\,\mathrm{MHz}$ from the definition of q in (14). The particles' initial conditions were generated at random, but confined to be within $10\,\mu$m of the center of the trap.

C. FORTRAN Implementation

The programming language of choice was FORTRAN. The main routine simulates the interaction between an arbitrary number N of positrons and N' of antiprotons, evolving the equations of motion (17) and (18) by making calls to a numerical integrator of our choice. We carefully investigated the Euler, Runge-Kutta, and Velocity Verlet algorithms [18]. However, these methods were found to be inefficient for our simulations due to the vast changes in magnitude of the spatial separation of particles. Since particles may be as far away as several tens of μm and may approach as closely as several nm, we found it prudent to employ an integrator capable of accommodating large variations in length-scales.

The accuracy delivered by conventional numerical integration routines is determined predominantly by the size of the time step taken by the controlling program. This imposes a limit on the efficiency of our simulations, which we ran on a 2.1 GHz Intel Core 2 Duo processor. For example, when increasing the number of particles in our trap, we increase the number of coupled differential equations. To maintain the same degree of accuracy that we achieved for a fewer number of coupled equations, we require a smaller step size due to the smaller average separation between particles. Thus, integrators with a fixed step size will work, but become more and more inefficient as one increases the accuracy. In order to overcome this obstacle, we implemented a 4th order Runge-Kutta method with 5th order adaptive step-size control [18]. This algorithm allows specification of the required accuracy and the integrator adjusts the size of the time steps dynamically during the integration to ensure that the specified accuracy requirement is met.

In order to detect antihydrogen formation, we solve the two-body reduced-mass problem [19] for each positron-antiproton pair along their trajectories $\mathbf{r}_i(t)$, $\dot{\mathbf{r}}_i(t)$, $\mathbf{R}_k(t)$, and $\dot{\mathbf{R}}_k(t)$. We compute the associated principal quantum number

$$n(t) = \sqrt{\frac{-R}{E(t)}}, \tag{19}$$

where $R = 13.6\,\mathrm{eV}$ is the hydrogen Rydberg constant and $E(t)$ is the *classical* energy of the equivalent reduced-mass particle determined from the numerical solutions of (17) and (18). It is important to realize that $n(t)$ is a sensitive enough function of $E(t)$ that approximating the mass of the antiproton as infinite is not sufficient—the correct, finite mass must be used. Of course, a principal quantum number according to (19) exists only for $E(t) < 0$. For $E(t) > 0$ the associated positron-antiproton pair is not in a mutual bound state, no antihydrogen has formed, and the corresponding pair is not considered at this particular time t. A plot of $n(t)$ versus time for any positrons orbiting a parent antiproton allows us to determine if antihydrogen has been produced. A plateau in $n(t)$ corresponds to a bound pair (formed antihydrogen). Our simulations show that $\bar{\mathrm{H}}$ is preferentially produced in high Rydberg states, i.e. $n(t)$ is large (typically on the order of $n(t) \approx 100$).

IV. RESULTS

Our earliest attempts consisted of a single positron and a single antiproton with initial positions within $10\,\mu$m of the center of the trap. Since the potential in the Paul trap is time-dependent, the energy of the particles is not conserved [19]. Thus, our working hypothesis was that antihydrogen could be formed via "field-assisted recombination." This process may be understood in analogy to the known process of three-body recombination, in which a third particle interacts with a particle pair. In doing so, the third particle removes enough energy and angular momentum to force the original particle pair into a bound state. In our envisioned field-assisted recombination process, the field itself would play the role of the third particle. To test this, we conducted simulations of a single particle of either species. Within times comparable to those that it took to synthesize Rydberg $\bar{\mathrm{H}}$ with other initial trap conditions, we did not find the field-assisted recombination effect sufficient to form antihydrogen. If this effect exists, it is either negligible, or a theoretical or computational demonstration requires a quantum mechanical approach. Another consideration is that the field near the center of the trap is very weak. It may be that the effect is proportional to cloud size: a larger cloud would require more particles to be interacting with the strongly varying part of the field. However, for many particle clouds, the field-assisted recombination effect, if it exists, would be difficult to separate from N-body recombinations.

Next, we simulated a scenario that would perhaps be the most conducive to experimental implementation: injecting an antiproton into a cloud of positrons already confined close to the center of the trap, but not crystallized [13]. Even when the initial speed of the antiproton was made very small, the energy it gained upon entry into the positron cloud took a long time to dissipate on the time scale of our simulation, which corresponds to only about 0.5 ms. The dominant motion of the antiproton was an oscillation between its starting position in the trap and a position diametrically opposite. Despite the large-amplitude oscillations, there was still some interaction with the individual positrons. Due to inelastic collisions, we did see the oscillation amplitude of the antiproton decrease somewhat over time. While we did not observe antihydrogen production in this scenario, we did confirm a new trapping mechanism. Even with trapping parameters optimized for positron confinement, binding of the negatively charged antiprotons to the positively charged positron cloud leads to strong antiproton trapping. This is one of the central results of our research.

Based on the new space-charge trapping mechanism, we conjecture that if we were able to simulate the an-

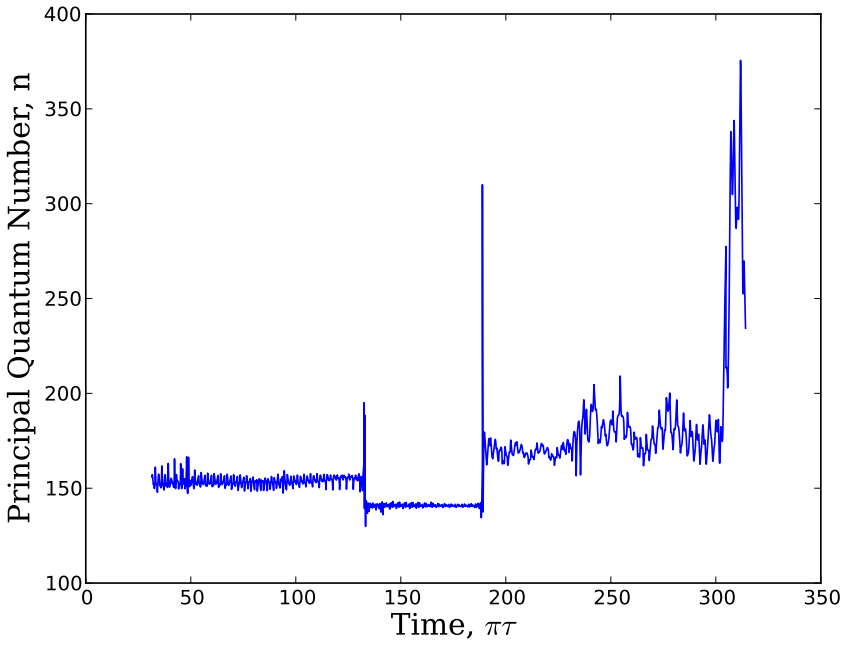

FIG. 2. Plot of the principal quantum number $n(t)$ as a function of time for one of our recombination events. On the x-axis is scaled time, $t_* = \pi\tau$, where τ is the number of trap cycles. A plateau in $n(t)$, of about 30 ns duration, corresponds to transient $\bar{\mathrm{H}}$ formation.

tiproton's motion until it dissipated enough energy by inelastic collisions with the trapped positrons, the antiproton will be trapped within the positron cloud. The antiproton-positron cloud system will always be focused into the center of the trap due to the positron-optimized trapping parameters. The conjectured energy dissipation is motivated by the fact that while, from a distance, the positron cloud looks like a uniform charge distribution, when an antiproton passes through the cloud and interacts with the individual positrons, it imparts kinetic energy to them. This process will heat up the positron cloud, but it allows the antiproton to come within range of recombination with a relatively small amount of kinetic energy.

With these results and ideas in mind, we proceeded to simulate a third scenario, where the antiproton was already cooled and bound within the positron cloud. We found that transient recombination of positrons and antiprotons into $\bar{\mathrm{H}}$ indeed occurs in the Paul trap. The two specific cases in which we observed $\bar{\mathrm{H}}$ formation consisted of 10 positrons and either 1 or 2 antiprotons. In Fig. 2, as an example, we show the principal quantum number $n(t)$ versus time for one of our observed recombination events. The regions of the graph where the principal quantum number fluctuates significantly correspond to unbound positron-antiproton pairs of various energy levels. However, we also observe a plateau in $n(t)$, of about 30 ns duration, which corresponds to transient $\bar{\mathrm{H}}$ formation in a highly excited Rydberg state.

V. CONCLUSIONS AND OUTLOOK

In this paper we present two fundamentally new and important results. Firstly, our simulations prove that antiprotons and positrons can be simultaneously confined in a Paul trap, due to Coulomb interactions. This is important, because a Paul trap optimized for the storage of positrons is not, by itself, capable of efficient antiproton storage, due to the large mass difference between the two particle species. Secondly, our simulations show that the Paul trap is indeed a viable candidate for synthesizing $\bar{\mathrm{H}}$. While the formed anti-atoms are subsequently destroyed by positron-$\bar{\mathrm{H}}$ collisions, we conjecture that the lifetime of $\bar{\mathrm{H}}$ atoms formed in the Paul trap may be increased greatly by accounting for radiative decay into lower-n states, which results in more strongly bound $\bar{\mathrm{H}}$ atoms that are less susceptible to destruction by collision with positrons.

Looking towards the future, we note that the Paul trap may be able to produce $\bar{\mathrm{H}}$ atoms, but it is not capable of storing them, because $\bar{\mathrm{H}}$ is a neutral particle. Therefore, the produced $\bar{\mathrm{H}}$ atoms have to be guided out of the Paul trap and stored in a suitable neutral-particle trap. Several different trap designs are available for achieving this goal; we present the following possibility.

Recent experiments have shown that it is possible to trap neutral atoms in the vortex formed by a (Type-II) superconducting microstructure in its mixed state [20, 21]. We hypothesize that $\bar{\mathrm{H}}$ should be no excep-

tion. These vortex traps are presently pursued with atom-optical systems in mind: they open new frontiers for atom optics [20, 21], perhaps in just the way necessary to move forward with $\bar{H}$ experimentation. This type of trapping procedure would allow us to cool the $\bar{H}$ even further via Doppler cooling and obtain a direct optical confirmation of the anti-atoms via the scattered light. The difficulty will be in transitioning to the vortex trap from the Paul trap. However, it may be possible that the same magnetic field used to create the Abrikosov vortex could shuttle $\bar{H}$ out of the Paul trap and into the vortex trap. Preliminary experiments with hydrogen atoms (more practical, at present, than experiments with $\bar{H}$) may be preformed to explore the prospects of trapping antihydrogen in Abrikosov vortices.

VI. ACKNOWLEDGEMENT

Guy Geyer would like to thank the Wesleyan University Physics Department as well as the American Physical Society Committee on Minorities in Physics for generous grants to support his undergraduate research in the summer of 2010.

[1] R. G. Lerner and G. L. Trigg, *Encyclopedia of Physics*, 2nd edition (VCH Publishers, New York, 1991).
[2] P. Morrison, Am. J. Phys. **26**, 358 (1958).
[3] L. I. Schiff, Phys. Rev. Lett. **1**, 254 (1958).
[4] M. Villata, Europhys. Lett. **94**, 20001 (2011).
[5] A. Kellerbauer *et al.* Nucl. Instrum. Meth. B **266**, 351 (2008).
[6] E. F. Taylor and J. A. Wheeler, *Spacetime Physics*, 2nd edition (Freeman, New York, 1992).
[7] G. B. Andresen *et al.*, J. Phys. B: Atomic, Molecular and Optical Physics **41**, 011001 (2008).
[8] C. Amole *et al.*, Nature, **483**, 439-443 (2012).
[9] G. Gabrielse *et al.*, Phys. Rev. Lett. **89**, 2 (2002).
[10] G. Gabrielse *et al.*, Phys. Rev. Lett. **100**, 1 (2008).
[11] G. B. Andresen *et al.*, Nature Physics **7**, 558 (2011).
[12] W. Paul, Rev. Mod. Phys. **62**, 531 (1990).
[13] R. Blümel, J. M. Chen, E. Peik, W. Quint, W. Schleich, Y. R. Shen, and H. Walther, Nature **334**, 309 (1988).
[14] J. Hoffnagle, R. G. DeVoe, L. Reyna, and R. G. Brewer, Phys. Rev. Lett. **61**, 255 (1988).
[15] D. J. Griffiths, *Introduction to Electrodynamics*, 3rd edition (Prentice Hall, Upper Saddle River, 1999).
[16] Abramowitz M and Stegun I A 1964 *Handbook of Mathematical Functions* (Washington DC: National Bureau of Standards) p 722
[17] H. G. Dehmelt, Adv. Atom. Mol. Phys. **3**, 53 (1967).
[18] W. H. Press, S. A. Teukolsky, W. T. Vetterling, and B. P. Flannery, *Numerical Recipies in Fortran*, 2nd edition (Cambridge University Press, Cambridge, 1996).
[19] J. B. Marion and S. T. Thornton, *Classical Dynamics of Particles and Systems*, 4th edition (Harcourt Brace, Fort Worth, 1995).
[20] B. Zhang, R. Fermani, T. Müller, M. J. Lim, and R. Dumke, Phys. Rev. A **81**, 063408 (2010).
[21] F. Shimizu, C. Hufnagel, and T. Mukai, Phys. Rev. Lett. **103** 253002 (2009).

Measurement of the Speed and Energy Distribution of Cosmic Ray Muons

Grant Remmen[1, a] and Elwood McCreary[1, b]

[1] *Department of Physics, School of Physics and Astronomy, University of Minnesota, 116 Church Street SE, Minneapolis, MN 55455, USA*

The time of flight distribution of cosmic ray muons was measured for various spacings of detectors filled with plastic scintillator, allowing for a determination of the mean speed, as well as constraint of the energy spectrum below $0.95c$. The use of a time-to-amplitude converter allowed for precise timing measurements and resolution of the shape of the timing distribution for each spacing, necessary for constraining the energy spectrum. The mean speed of cosmic ray muons was found to be $(2.978 \pm 0.007) \times 10^8\,\mathrm{m\,s^{-1}} = (0.993 \pm 0.002)\,c$. The energy spectrum below 0.34 GeV was found to be consistent with a flat distribution and was parameterized with a power law of the form $n(E)\,dE \propto E^{-\alpha} dE$, with α best fit by $(-7.9 \pm 9.1) \times 10^{-4}$.

Keywords: cosmic rays, elementary particles: muons, energy spectrum, relativistic velocity measurement, scintillation detector, nanosecond timing measurement, astroparticle physics, special relativity

I. INTRODUCTION

Cosmic rays, energetic particles from deep space that penetrate Earth's atmosphere, were discovered in 1912 by Victor Hess through the use of a balloon-borne electroscope. Consisting primarily of energetic protons and nuclei produced by supernovae, cosmic rays are constrained by the Galactic magnetic field, forming a relativistic gas with particle energies of up to 10^{21} eV.[6] Upon entering the atmosphere, the primary cosmic rays interact and decay through various other particle species, changing the population from hadrons to leptons, such as muons, which were first detected by cosmic ray physicist Bruno Rossi in 1932.

The very existence of muons at sea level indicates the effects of special relativity. A second generation lepton with properties analogous to the electron, muons have rest mass m_μ of $105.7\,\mathrm{MeV}/c^2$ and rest frame lifetime $\tau \approx 2.2\,\mu$s. Experimental evidence indicates, however, that muons are produced high in the atmosphere, with travel time to sea level much greater than τ in the rest frame of the Earth. The $\sim$ GeV energies of cosmic ray muons at sea level[11] imply speeds greater than $0.999c$, so that relativistic time dilation must be taken into account.

In this experiment, a time-to-amplitude converter (TAC) was used to measure the muon time of flight between detectors, which was on the order of a few ns. This device allowed for more precise measurement of the timing distribution than was obtained in prior measurements of cosmic ray muon speeds at MIT and the University of Minnesota.[2,6] In these prior experiments, the distribution was parameterized by a single speed and was limited in precision ($\sim 10\%$ relative error for Ref. 6). Finally, three scintillator paddles were used for coincidence testing; the use of three paddles decreased the total solid angle over which muon events were collected, which led to greater precision of the measurement. The three-paddle configuration also lessened the probability of independent random background events being incorrectly counted, thereby improving the reliability of the result.

II. THEORY

The special theory of relativity, developed by Einstein over a century ago, governs the behavior of objects moving at relativistic speeds. In particular, Lorentz contraction and time dilation imply that observers will see distances and times in frames in motion relative to them contracted (respectively, lengthened) by factors of $1/\gamma$ and γ, where $\gamma \equiv 1/\sqrt{1-(v/c)^2}$.[10] With relativity taken into account, a muon with $E = 4\,\mathrm{GeV}$ has $\gamma \approx 38$. Hence, the lifetime of the muon, as seen from the Earth, is $\gamma\tau \approx 83\,\mu$s, allowing 4 GeV muons to reach the surface from a height of over 20 km. The observation of the speed of cosmic ray muons, which is close to c, provides an interesting opportunity to observe massive particles in the relativistic limit.

In order to determine the mean speed of cosmic ray muons, a linear fit was calculated. The average time t_{obs} between detections of a muon in paddles separated by a given vertical distance y was measured. This vertical spacing corresponds to an average muon path length l, as not all muons are vertically incident. With l plotted as a function of t_{obs}, the resulting line has slope equal to the mean speed v_μ and the horizontal intercept t_{delay} corresponds to the inherent delay in the detectors and cables:

$$l = v_\mu \left(t_{\mathrm{obs}} - t_{\mathrm{delay}}\right). \tag{1}$$

Cosmic ray muons are not restricted to a single velocity, but are distributed in a spectrum of energies

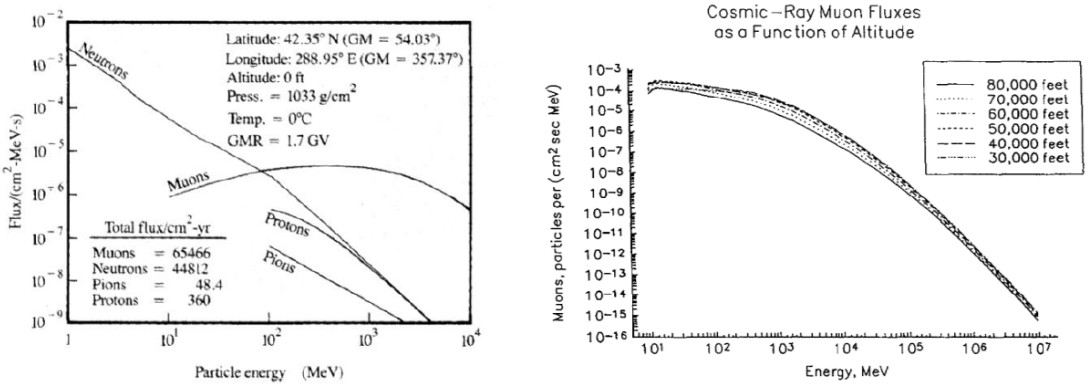

Figure 1: Examples of prediction for various cosmic ray fluxes (figures reproduced from Refs. 12 and 7). Note that the muon distribution does not vary strongly with energy below 1 GeV and is dependent on geographical and atmospheric conditions, such as altitude, location, pressure, etc.

(see Fig. 1). For cosmic ray muons below 1 GeV, the energy spectrum is fairly flat.[4] This statement may be parameterized by a power law:[1]

$$n(E)\,dE \propto E^{-\alpha}dE \implies n(v)\,dv \propto \gamma^{3-\alpha}v dv. \quad (2)$$

The conversion to the velocity distribution follows from the relation $E = \gamma m_\mu c^2$. For a given mean path length l, Eq. (2) may be converted into an expected timing distribution:

$$n(t_{\rm bin})\,\Delta t_{\rm bin} \propto l^2 t_{\rm bin}^{-3}\left(1 - \frac{l^2}{c^2 t_{\rm bin}^2}\right)^{\frac{\alpha-3}{2}} \Delta t_{\rm bin}, \quad (3)$$

where $t_{\rm bin}$ is the time corresponding to a given bin and $\Delta t_{\rm bin}$ is the bin width. By comparing the observed timing distributions with expectations derived from Eq. (3), a fit for the parameter α can be found. In this way, a characterization of the cosmic ray muon velocity distribution allows for constraints to be placed on the energy spectrum.

There exist several sources of uncertainty in the measurement of the mean speed of cosmic ray muons. The angular distribution of cosmic rays follows the empirical relation

$$I = I_0 \cos^n \theta \quad (4)$$

where θ is the zenith angle, I_0 is the flux (counting rate) per unit area per unit solid angle for vertically incident muons, and $n \approx 2$.[5] Angular distribution is a source of uncertainty in measurements of muon speed, due to the variation in possible path lengths. In addition, the variance in path length traversed by signals propagating within the scintillator paddles contributed another source of error in the timing distribution for a given paddle spacing. Other sources of error included electronic jitter and thermal noise in the apparatus. These sources of uncertainty are treated in greater detail in Section IV.

III. EXPERIMENTAL APPARATUS AND METHODS

This experiment involved analyzing the observed time differences between light pulses generated by cosmic ray muons interacting with plastic scintillator material, which was encased in light-tight paddles (see Fig. 2). These pulses were transformed into electrical signals and amplified by photomultiplier tubes (PMTs) to voltages on the order of 10^{2-3} mV. For the scintillator paddles and PMTs used in this experiment, which possess improved sensitivity over those used in Ref. 2, the optimum operating voltages (on the order of -1 kV) had been previously determined. Three scintillator paddles were used, labeled A, B, and C from top to bottom; the perpendicular distance y between paddles A and B was varied among seven different spacings by mounting the paddles on the rungs of a ladder and varying the position of paddle B. For each spacing, data was taken with integration time of approximately 24 hours at a minimum.

The direct signal of a PMT is short in duration, on the order of a few ns, and the shape of the signal pulse is curved, not containing a clean rising or falling edge. In order to produce a longer square pulse more suited to analysis in NIM-standard logic, the signal of each PMT was input into a LeCroy 821 Quad Discriminator. When the PMT voltage exceeds the minimum threshold of 31.5 ± 1.5 mV, the discriminator outputs a square pulse; pulse widths of 64, 24, and 27 ns were used for the outputs of scintillator paddles A, B, and C, respectively. The outputs of the discriminators were used to create in-

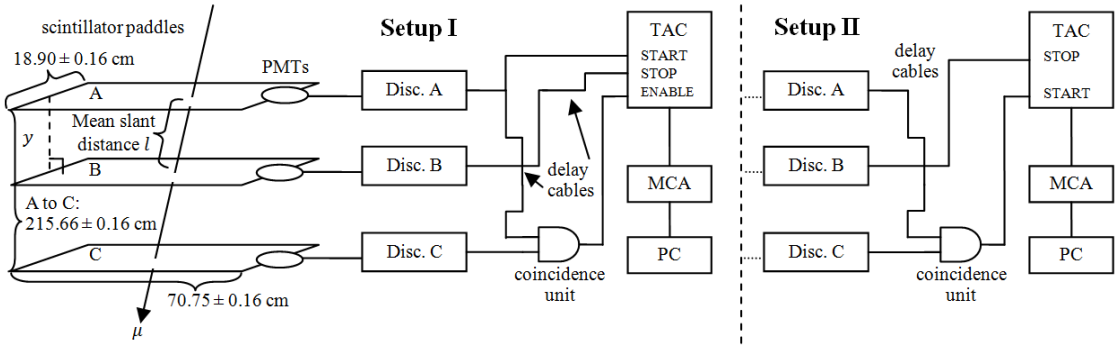

Figure 2: Experimental apparatus for the measurement of the speed of cosmic ray muons, using coincidence Setup I (left) and II (right). Three scintillator paddles (far left) are mounted on a ladder at different spacings. When a muon passes through the paddles, signals from the photomultiplier tubes (PMTs) are re-output by discriminators (Disc.). The time-to-amplitude converter (TAC) measures the interval between events at A and C (plus t_{delay}) and the resulting voltage is input to the multichannel analyzer (MCA) and recorded on a computer (PC).

puts for the START and STOP lines of an ORTEC 566 TAC, which outputs a voltage pulse proportional to the time difference between input pulses. These voltages were then binned and stored using an ORTEC EASY-MCA 1,024-bin multichannel analyzer (MCA), which transferred the data to a computer.

Three-paddle coincidence testing was used both to reduce the probability of a measurement being triggered by independent, unrelated muons and to decrease the relevant solid angle for small y. Complete data sets were taken for two different implementations of the coincidence test (see Fig. 2 for schematics). In Setup I, the clean pulses generated by the discriminators for paddles A and C were input to a C.A.E.N. Model N455 Quad coincidence logic unit (essentially an AND gate), the output of which was sent to the ENABLE line of the TAC. The output from A was sent directly to the START line of the TAC, while the signal from B, delayed by 46 ns using coaxial and LEMO cables, was sent to the STOP line. The signal from paddle A to the AND gate was delayed by a 36 ns coaxial cable, to ensure that it arrived after the signal from C. It was found that Setup I produced significant noise peaks in the timing distribution at high values of y.

In Setup II, which produced less noisy data, the signals from paddles A and C were input into a coincidence gate as before. The signal from A was delayed by a 14 ns LEMO cable, so that, as in Setup I, the signal from A always arrived after C. The coincidence signal was input into the START line of the TAC, with no ENABLE used. The TAC used in this experiment has an inherent limitation on the range of times it can measure: any measurement must be in excess of 10 ns. Therefore, as in Setup I, it was necessary in Setup II to delay the signal from paddle B; in order to accomplish this, B was input to the STOP line with a 36 ns coaxial delay cable. In both Setups I and II, all electronic components were matched at 50 Ω impedance.

As a result of the coincidence tests, this experiment required triple coincidence ($\mathrm{A} \wedge \mathrm{B} \wedge \mathrm{C}$) for a muon to be counted. Following the reasoning of Ref. 8, the expected number of background counts in each bin in our experiment is

$$N_{\mathrm{b}} = 3 n_{\mathrm{A}} n_{\mathrm{B}} n_{\mathrm{C}} T_{\mathrm{tot}} \Delta t_{\mathrm{bin}}^2, \tag{5}$$

where n_{A}, n_{B}, and n_{C} are the count rates in paddles A, B, and C individually (over the solid angle subtended by A and C), T_{tot} is the integration time, and Δt_{bin} is the timing width of a bin (approximately 49 ps). With the total observed background rates of approximately 50 Hz for A and B and 25 Hz for C, $N_{\mathrm{b}} \ll 1$, even for integration times of several days.

The mean path length is dependent on the geometry of the scintillator paddles and the angular distribution of cosmic ray muons, given in Eq. (4). A Monte Carlo simulation was used to calculate the mean path length l for varying y. Pseudorandom coordinates were generated for the location of muon incidence on the top paddle, as well as for the azimuth and zenith angles of the muon's velocity vector. If the muon's trajectory intersected paddles A, B, and C, the muon was ruled successful and l was computed geometrically. After generating 10^5 successful muons for each spacing y between paddles A and B at 1 mm intervals, l was known to a precision on the order of 10^{-6} for a given value of y. Due to the constant solid angle formed by paddles A and C, the relation is well represented by a linear scaling of the perpendicular distance. In Setups I and II, respectively, $(l - y)/y$ was fit as $(9.0001 \pm 0.0007) \times 10^{-3}$ and $(8.9503 \pm 0.0007) \times 10^{-3}$, with the difference be-

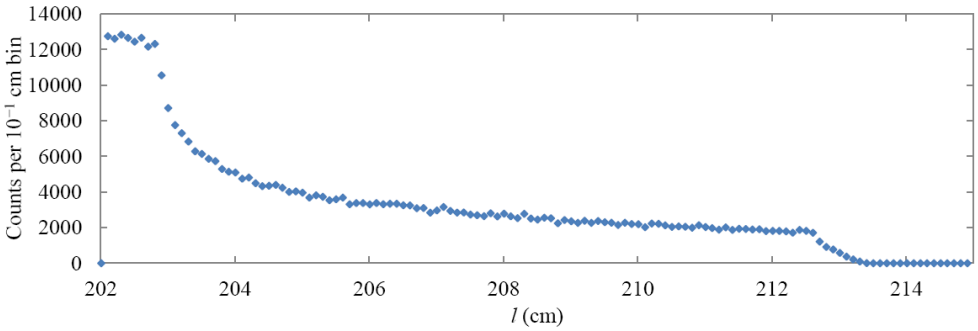

Figure 3: Distribution of accepted lengths from a Monte Carlo simulation of over 4×10^5 muons, with normal spacing y of 202.009375 cm.

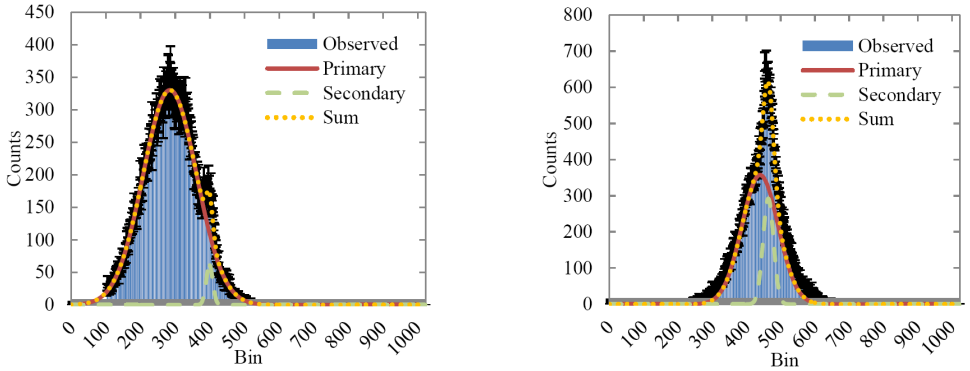

Figure 4: The timing distribution for a mean slant length of 115.80 ± 0.16 and 114.64 ± 0.16 cm for integration times of 48.6 and 50.9 hours, from Data Set I (left) and II (right), respectively. Multiple Gaussian fits for the peak regions of the observed timing distribution (above 20% and 60%, respectively, of the smoothed peak height) are also shown. The reduced χ^2 values for the fits shown are 1.14 and 1.41 for I and II, respectively.

ing due to the 0.64 cm variation between the two Setups of the perpendicular distance between paddles A and C. Though small, in effect lengthening the mean path length by less than 1% over the perpendicular distance y, this correction factor is necessary for an accurate determination of muon speed, given the level of precision in our experiment. A length distribution for a particular y, from a simulation of over 4×10^5 virtual muons, is shown in Fig. 3. Additional Monte Carlo simulations were conducted to assess the effect of misalignment (e.g. paddle B not directly aligned with A and C). It was found that this effect introduces relative errors on the order of 10^{-5} or smaller, which are dwarfed by the 0.16 cm uncertainties in y itself, which was measured directly.

IV. ANALYSIS AND RESULTS

Before the spectrum of speeds (equivalently, energies) could be fit, it was necessary that the inherent delay t_{delay} in the apparatus be found. This was possible by performing a linear fit between the set of mean distances l and the representative times for the respective timing distributions, effectively finding the mean speed of the observed cosmic ray muons. Since the observed timing distributions were non-Gaussian, a multiple (two or three) Gaussian fit was used to parameterize their shapes. In all fits over timing distributions, the error in a particular bin with N counts was taken to be $\sqrt{N}$, by Poisson statistics. Due to the long tails of the distributions, the range of data used for these fits was restricted to the subset with count totals above 20% or 60% of the peak of the distribution for Data Sets I and II, respectively; the eligible regions above the threshold were found by smoothing the data with a local average over five bins. This fitting procedure produced reduced χ^2 values between approximately 1.1 and 2.2 for Data Set I and between 0.8 and 1.4 for Data Set II, indicating fairly good correspondence between the shapes of the timing distributions and those of the fits (see Fig. 4).

For each fit, the peak of the primary Gaussian was taken to correspond to the mean time of flight between paddles A and B for muons passing through the apparatus. For Data Set II, the primary Gaussian corresponds to a shoulder feature near the peak

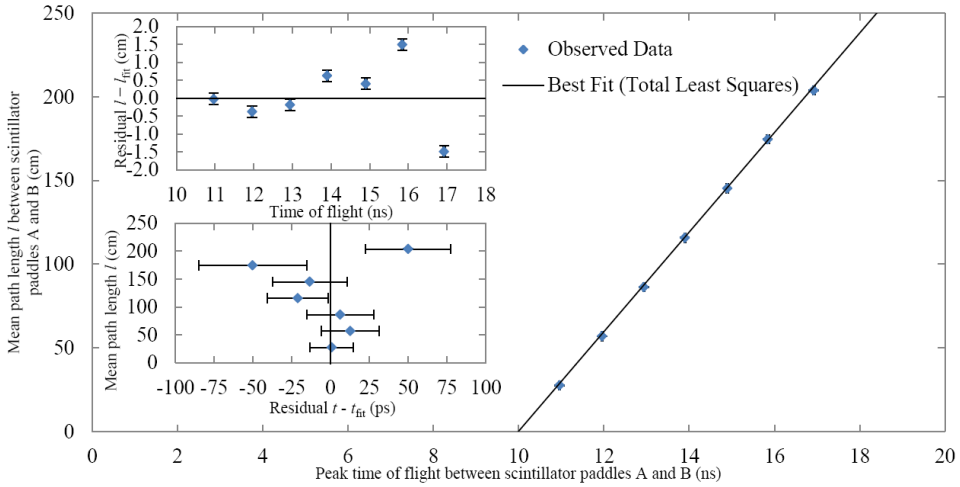

Figure 5: Total least squares linear fit for the mean speed of cosmic ray muons, based on Data Set I. Also shown are the residuals in time and distance, illustrating the quality of the fit, as well as the absence of any obvious systematic trends.

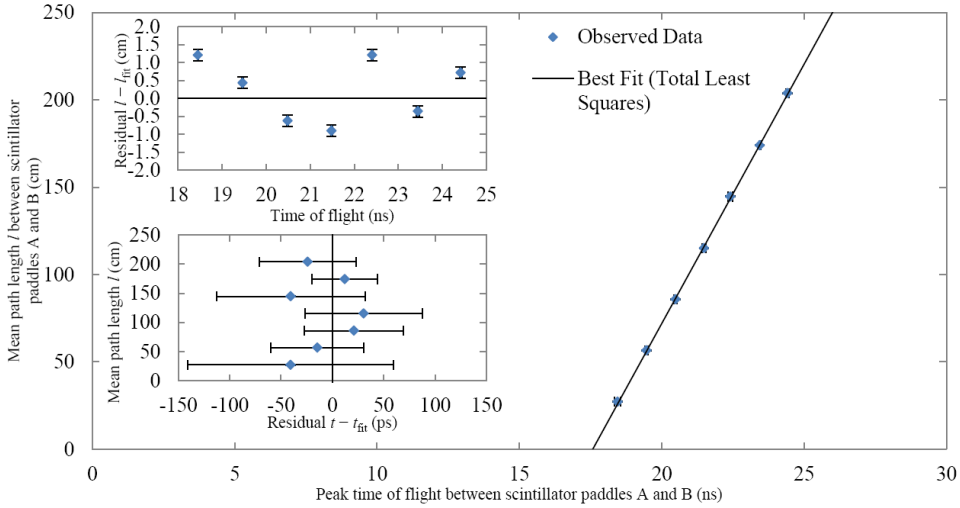

Figure 6: Total least squares linear fit for the mean speed of cosmic ray muons, based on Data Set II. The residuals in time and distance are also plotted, indicating goodness of fit and a lack of clear systematic trends.

(see Fig. 4). In Data Set I, the secondary Gaussian corresponds to a noise peak, possibly due to an internal reflection in the wiring, appearing at nearly the same bin for each spacing. The secondary Gaussian in Data Set II parameterizes the non-Gaussian shape of the distribution, though its origin remains unclear.

The error in the fit time was found using the $\chi^2{+}1$ method, i.e. varying the mean in both directions until χ^2 is increased by unity. The relative errors in both time and length are on the order of 10^{-3}. Due to the comparable size of the errors in length and time, a linear fit among the seven data points required the implementation of the total least squares method, detailed in Ref. 9. Since this method is not analytically tractable for general errors, the parameters v_μ and t_{delay} were numerically varied until χ^2 was minimized, with the $\chi^2 + 1$ method used for error estimation. For Data Set I, the best fit mean speed was $v_\mu = (2.983 \pm 0.002) \times 10^8\,\text{m}\,\text{s}^{-1} = (0.9950 \pm 0.0006)\,c$ and the timing offset was $t_{\text{delay}} = 10.036 \pm 0.008\,\text{ns}$ (see Fig. 5). For this fit, the reduced χ^2 value was 1.43 for 5 degrees of freedom, at 21% probability. The linear speed fit for Data Set II yielded $v_\mu = (2.969 \pm 0.002) \times 10^8\,\text{m}\,\text{s}^{-1} = (0.9902 \pm 0.0008)\,c$. For configuration II, the timing delay in the apparatus was best fit with $t_{\text{delay}} = 17.57 \pm 0.02\,\text{ns}$ (see Fig. 6). The reduced χ^2 value for

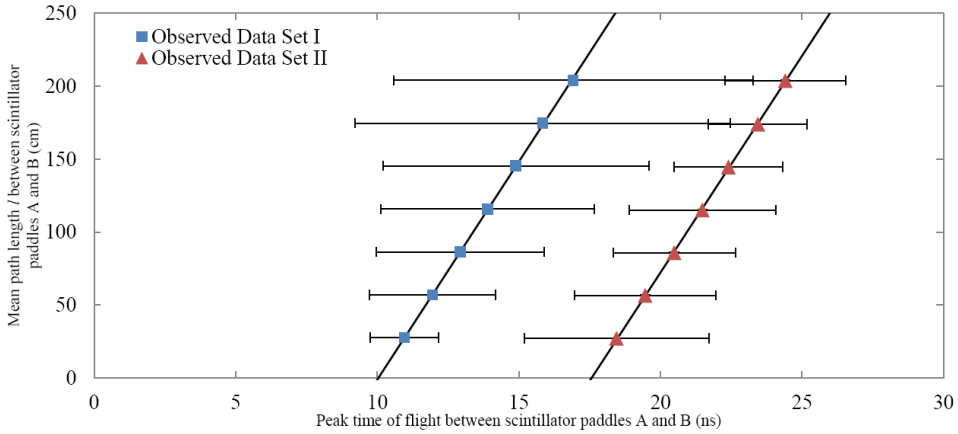

Figure 7: Total least squares linear fit for the speed distribution width of cosmic ray muons, based on Data Sets I and II. The error bars reflect the full widths of the primary Gaussian curves from the multiple Gaussian fits and are overestimates of the true dispersions in the timing distributions caused by velocity variation.

the total least squares fit of Data Set II was 0.29, at 8% probability.

Before calculating the true distribution of velocities, it is instructive to examine what one would obtain for the width of the velocity spectrum, if the errors in the mean time for each spacing are simply taken to be the widths of the Gaussians fit to the timing distributions. Though this method provides an overestimate of the width of the speed distribution, it yields a sense of the tightness of the constraints placed on the distribution by our measurement. In this case, a total least squares fit yields $v_\mu = \left(2.99^{+0.25}_{-0.21}\right)\times 10^8\,\mathrm{m\,s^{-1}} = 0.996^{+0.084}_{-0.072}\times c$ for Data Set I and $v_\mu = \left(2.97^{+0.12}_{-0.11}\right)\times 10^8\,\mathrm{m\,s^{-1}} = 0.991^{+0.039}_{-0.036}\times c$ for Data Set II (see Fig. 7). In this way, our results yield tighter constraints on the speed of cosmic ray muons than other measurements of muon speed in undergraduate laboratories.[2,6]

Finally, the energy spectrum parameter α (see Eq. (2)) can be calculated by an analysis of the shape of the timing distributions. However, the timing distributions observed (as in Fig. 4) are not direct representations of the expected function of Eq. (3). Rather, the timing spectrum in Eq. (3) was convolved (i.e. blurred) with all the sources of error in this experiment. These sources of error included the variance in path length depicted in Fig. 3, as well as thermal noise, jitter in the electronics, variance in the lengths of paths of propagation within the scintillator paddles, and other sources of uncertainty; in effect, these multiple error sources were themselves combined in convolution to give a total effective resolution for our timing distributions.

The total resolution from the combined errors may be parameterized by a Gaussian kernel, though the individual sources are non-Gaussian. The kernel was fit from the timing distributions above a threshold of 25% of the smoothed peak, over bins such that $ct_{\mathrm{bin}} < l$, so that the counts observed in those bins could not correspond to physical particle detections. It is important to note that the method of fitting the Gaussian kernel does not account for systematic errors, such as deviation from expectations of the dependence of muon flux on zenith angle (i.e. $I \propto \cos^n\theta$, with $n \neq 2$) and errors in the tape measure used to determine the perpendicular spacing. The kernels were well fit by Gaussians for Data Set I, with reduced χ^2 values between 0.9 and 1.4; the kernel region of Data Set II was less well fit by Gaussians, with reduced χ^2 ranging from 1.1 to 4.2. For each spacing l, the Gaussian kernel, after being normalized to unit area, was numerically convolved with the distribution given in Eq. (3), with the time for a given bin (t_{obs}) corrected to an absolute time by subtracting t_{delay}. The amplitude of the spectrum was numerically fit for each timing distribution by minimizing χ^2; in this case, analytical fitting of the amplitude was not practicable, due to divergence of the integral of Eq. (3).

The exponent α in the spectrum was fit numerically over all spacings simultaneously by minimizing the total χ^2, with uncertainty found using the χ^2+1 method. In this experiment, α was fit over bins corresponding to muon speeds less than $0.95c$, since the power law exponent is very different at higher energies, where the spectrum is no longer nearly flat. Sample fits for two representative timing distributions are shown in Fig. 8. For Data Set I, it was necessary for the noisy region of the data to be excluded from fitting; the fit for Data Set II appears in good visual agreement with the observed timing distribution.

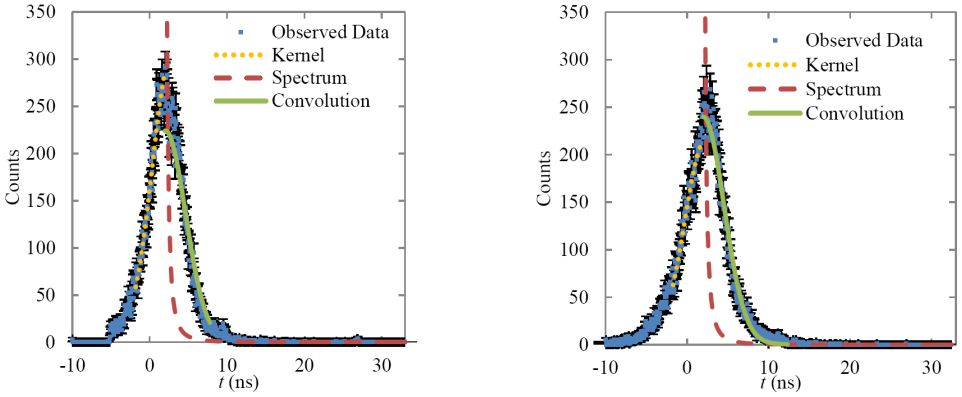

Figure 8: Examples of spectrum fitting for mean slant lengths of $56.94 \pm 0.16\,\mathrm{cm}$ (left) and $56.62 \pm 0.16\,\mathrm{cm}$ (right) for Data Sets I and II, respectively. The observed data are plotted, with t_{bin} corrected by t_{delay}. Also shown are the curves for the Gaussian kernel fitting, the theoretical, noise-free curve from Eq. (3), and the convolution of the pure timing spectrum with the Gaussian resolution.

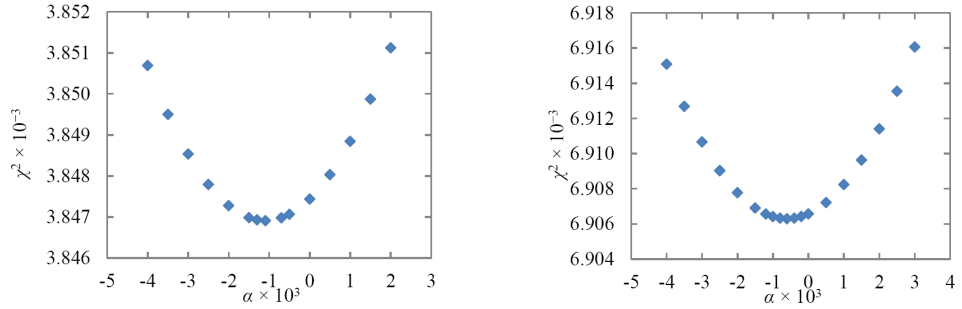

Figure 9: The effect on χ^2 as the energy distribution power law exponent α is varied, for the fit of Data Sets I (left) and II (right). In both cases, the behavior is quadratic, with the minimum at the best fit value of α.

For these fits, the Poisson error in the number of counts in a given bin dominated over the uncertainty in the absolute time. The method used for analyzing the timing distributions assumes that the resolution is the same for fast and slow muons, i.e. that the Gaussian kernel width is constant over the timing distribution. This is the most straightforward *a priori* assumption that allows for the finite resolution of the timing measurement to be taken into account. For Data Set I, the best fit value of α was found to be $(-1.1 \pm 1.5) \times 10^{-3}$, with a reduced χ^2 value of 3.84 over 1,001 degrees of freedom. The fitting process for Data Set II, where the noisy regions of Data Set I did not require exclusion, yielded $\alpha = (-0.6 \pm 1.1) \times 10^{-3}$, for which the reduced χ^2 value was 4.21, with 1,641 degrees of freedom. For both Data Sets, the behavior of χ^2 upon varying α was investigated and found to be quadratic about the best fit value, as expected (see Fig. 9).

V. CONCLUSIONS

In this experiment, the mean speed of cosmic ray muons was measured using two independent implementations of the coincidence test, to a precision of $\sim 10^{-3}$. The χ^2 values for both linear fits were consistent with the number of degrees of freedom. The discrepancy between the mean speeds found from Data Sets I and II was $\Delta v_\mu = (1.4 \pm 0.3) \times 10^6\,\mathrm{m\,s^{-1}} = (4.8 \pm 1.0) \times 10^{-3} c$. The energy loss per unit atmospheric depth,[3] $\sim 2\,\mathrm{MeV\,g^{-1}\,cm^2}$, can only account for approximately $10^3\,\mathrm{m\,s^{-1}}$ of this discrepancy, based on differences in air pressure over Data Sets I and II. The velocity discrepancy was used as an estimate of the systematic uncertainty in our measurement: $\sigma_{v,\mathrm{sys}} = \Delta v_\mu / 2 = 7.1 \times 10^5\,\mathrm{m\,s^{-1}} = 2.4 \times 10^{-3} c$. In the interest of making a conservative estimate of the mean speed, this systematic uncertainty was applied to neither speed individually; instead, a weighted mean was taken over the two values of v_μ, with $\sigma_{v,\mathrm{sys}}$ added in quadrature in the uncertainty. This yielded a best combined value of

$v_\mu = (2.978 \pm 0.007) \times 10^8\,\mathrm{m\,s^{-1}} = (0.993 \pm 0.002)\,c$. In this way, no assumptions were made about which measurement was more reliable (if one Data Set were favored, the best value of v_μ would shift toward the value from that Data Set and the estimated error would be smaller). The best value of v_μ was consistent with an energy of 1 GeV and within approximately 2.6 standard deviations of the velocity (in excess of $0.999c$) corresponding to the mean ground level cosmic ray muon energy of $\sim 4\,\mathrm{GeV}$.[4] Furthermore, muon energy losses within the several floors of building material above our detectors can partially account for the slightly lower observed speed.

The behavior of the energy spectrum below $0.95c$ (0.34 GeV) was parameterized with a power law: $n(E) \propto E^{-\alpha} dE$; the velocity restriction ensures that higher energies were excluded, at which the energy spectrum changes to a different, steep power law. The two Data Sets yielded consistent values of α, with the best value of α calculated from a weighted mean of the two: $(-7.9 \pm 9.1) \times 10^{-4}$. This result is consistent with expectations of a nearly flat distribution Ref. 4, though more specific predictions are not available, due to the dependence of the muon energy spectrum on meteorological and geographic conditions, illustrated in Fig. 1. However, the reduced χ^2 values for the spectrum fitting were high for both Data Sets, with the largest discrepancies near the peak. This possibly implies that, contrary to predictions, the muon spectrum does not follow a single power law over the low energy range or, alternatively, that the timing resolution of our apparatus cannot be parameterized by a single Gaussian, independent of the time interval. In total, the results of this experiment demonstrate overall consistency with expectations regarding the mean speed and energy distribution of cosmic ray muons.

Acknowledgments

The authors are grateful for the advice of Professors Jeremiah Mans and Clem Pryke, as well as helpful conversations with Kurt Wick and Tanner Prestegard, University of Minnesota.

[a] Electronic address: remme024@umn.edu
[b] Electronic address: mccr0132@umn.edu

[1] Aglietta, M. et al. (1998). *Phys. Rev. D 58*(092005).
[2] Ahrens, M. and J. Bubola (2009). Mean velocity of cosmic ray muons. *Methods of Experimental Physics, University of Minnesota*.
[3] Dmitrieva, A., R. Kokoulin, A. Petrukhin, and D. Timashkov (2011). *Astropart. Phys. 34*(401).
[4] Eidelman, S., Particle Data Group, et al. (2004). *Phys. Lett. B 592*(1).
[5] Hall, R., D. Lind, and R. Ristinen (1970). *Am. J. Phys. 38*(1196).
[6] MIT Dept. of Physics (2010). *Lab Guide* (14).
[7] O'Brien, K. and W. Friedberg (1994). Terrestrial cosmic ray intensities. *Environment International 20*(645).
[8] Pearson, B. and D. Jackson (2010). *Am. J. Phys. 78*(491).
[9] Press, W., S. Teukolsky, W. Vetterling, and B. Flannery (1992). *Numerical Recipes in C*. Cambridge: Cambridge University Press.
[10] Rindler, W. (2001). *Relativity: Special, General, and Cosmological*. Oxford: Oxford University Press.
[11] Rossi, B. (1948). *Rev. of Modern Physics 20*(537).
[12] Ziegler, J. (1996). Terrestrial cosmic ray intensities. *IBM J. Res. Dev 40*(19).

A Geometrical Interpretation of Bell's Inequalities

Taylor Firman
University of Puget Sound

January 24, 2012

Abstract

Bell's Inequalities express constraints on the correlations of three random, binary variables and they can be applied to the interpretation of quantum mechanics. In an analysis of the theory behind these inequalities, this paper suggests a geometrical interpretation of Bell's Inequality in the form of a tetrahedron in "correlation space" to which correlation measurements are restricted. Using correlated photons produced through spontaneous parametric downconversion, we were able to experimentally demonstrate a set of measurements lying outside of this tetrahedron, negating the binary nature of hidden-variable theories.

1 Introduction

Quantum Mechanics is a statistical representation of nature in that we know the probability of specific physical characteristics of particles, but the particles themselves don't take on this characteristic until we objectively measure it, forcing the wavefunction to "collapse." This viewpoint generated controversy over the years and some rejected it in favor of a hidden-variable approach, stating that variables of which we are unaware determine characteristics of particles, not probabilistic wavefunctions. One example of hidden-variable theory was introduced by Einstein, Podolsky, and Rosen in 1935 through their EPR paradox, dealing with entangled particles.[1] Through this thought experiment, they reasoned that quantum mechanics either violates the principle of locality or is classified as incomplete, missing an additional element of reality to describe the system fully (i.e. a hidden variable). In response to this paradox, John S. Bell introduced numerical inequalities that restrict hidden variable systems but do not apply to quantum mechanical systems. Since this introduction, many experimental tests have demonstrated specific physical cases that violate Bell's Inequalities, therefore proving hidden-variable theories to be inaccurate descriptions of nature, and in 2002 specifically, Dietrich Dehlinger and Morgan Mitchell carried out one such experiment using correlated photons. By analyzing the theoretical implications of Bell's Inequalities, this study will introduce a graphical interpretation of these inequalities, and by replicating the experimental design of Dehlinger and Mitchell, the results will be applied within the interpretation.

2 Theoretical Context

Introduced in 1964, Bell's Inequality is a mathematical confirmation of quantum mechanics that disproves the validity of all hidden variable theories, no matter their complexity.[2] The theoretical context begins with a pair of correlated particles emitted from a single source, such as spin-$\frac{1}{2}$ particles or downconverted photons. Having come from a single parent source, these particles must have certain correlated characteristics such as spin or polarization, and knowing the state of one particle implies the state of the other. In our experiments, we used the process of Type-1 downconversion to produce two photons of identical polarization, so we will use this same context in the theoretical process. At either end of the source of correlated particles, detectors are placed to make some form of measurement, labeled A and B respectively. These detectors are given abstract orientations $\vec{a}$ and $\vec{b}$, and in the polarization context, an example of such an orientation would be the angle of a polarizer placed in front of a detector. As mentioned, a hidden variable, which we will denote as λ, is present throughout the entire process. After the emission of the correlated particles, enough distance separates the two particles so that communication between them is impossible, enforcing the assumption of locality. Therefore, after emission, λ is set in place, and if known, it determines any measurement outcome.

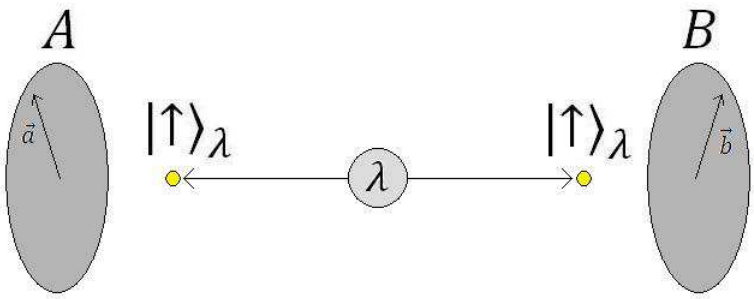

Figure 1: Theoretical set-up of photon emission towards detectors using particular orientations.

To illustrate this, consider the general case of a binary form of measurement, detection or non-detection at detector A using a single orientation $\vec{a}$ with hidden variable λ: $A(\vec{a}, \lambda) = \pm 1$, (+1 = detection; -1 = non-detection). Since the correlated photons maintain identical polarization, any measurement at detector B using orientation $\vec{a}$ will be identical to using $\vec{a}$ on detector A (i.e. $A(\vec{a}, \lambda) = B(\vec{a}, \lambda)$), so in an attempt to simplify concepts, theoretical measurement notation will only use detector A.

3 Mathematical Context

To analyze the mathematical relationship between the measurements made using two different orientations in the hidden variable context, we can analyze their statistical correlation between -1 (anticorrelation) and +1 (perfect correlation). By definition, the correlation between the measurements using $\vec{a}$ and measure-

ments using $\vec{b}$ is

$$C(\vec{a},\vec{b}) = \frac{\left\langle (A(\vec{a},\lambda)-\mu_{\vec{a}})(A(\vec{b},\lambda)-\mu_{\vec{b}})\right\rangle}{\sigma_{\vec{a}}\sigma_{\vec{b}}} \tag{1}$$

with μ_a, μ_b being the average values of $A(\vec{a},\lambda)$ and $A(\vec{b},\lambda)$ respectively, and σ_a, σ_b being the standard deviation of $A(\vec{a},\lambda)$ and $A(\vec{b},\lambda)$ respectively. However, since we are assuming uniform probability distribution for $A(\vec{a},\lambda)$ and $A(\vec{b},\lambda)$ and they can only take on values of ± 1, $\mu_{\vec{a}} = \mu_{\vec{b}} = 0$ and $\sigma_{\vec{a}} = \sigma_{\vec{b}} = 1$. This simplifies our correlation calculation down to

$$C(\vec{a},\vec{b}) = \left\langle A(\vec{a},\lambda)A(\vec{b},\lambda)\right\rangle, \tag{2}$$

the expectation value of the product of the two measurements.

Since one orientation gives us a measurement and two produce a correlation, Bell's Inequality takes the next logical step by using three orientations, $\vec{a}$, $\vec{b}$, and $\vec{c}$, to develop a mathematical relationship between correlations. Knowing that each of the three measurements using $\vec{a}$, $\vec{b}$, and $\vec{c}$ only have two possibilities (± 1), this leaves us with eight possible outcomes of all three measurements:

λ	$A(\vec{a},\lambda)$	$A(\vec{b},\lambda)$	$A(\vec{c},\lambda)$	P_λ
1	+1	+1	+1	P_1
2	+1	+1	-1	P_2
3	+1	-1	+1	P_3
4	+1	-1	-1	P_4
5	-1	+1	+1	P_5
6	-1	+1	-1	P_6
7	-1	-1	+1	P_7
8	-1	-1	-1	P_8

Table 1: Possible measurement outcomes using orientations $\vec{a}$, $\vec{b}$, and $\vec{c}$, along with associated λ index and probability.

By associating each possible outcome with a hidden variable index, λ, between 1 and 8, and a probability of occurring, P_λ, we can express the expectation value of the products of various measurements by using the summation notation of

$$C(\vec{a},\vec{b}) = \sum_{\lambda=1}^{8}\left[P_\lambda A(\vec{a},\lambda)A(\vec{b},\lambda)\right]. \tag{3}$$

To relate these values to one another, we can take the difference of two correlations using three orientations,

$$C(\vec{a},\vec{b}) - C(\vec{a},\vec{c}) = \sum_{\lambda=1}^{8}\left[P_\lambda A(\vec{a},\lambda)\left(A(\vec{b},\lambda) - A(\vec{c},\lambda)\right)\right], \tag{4}$$

and since $A(\vec{b},\lambda)^2 = 1$,

$$C(\vec{a},\vec{b}) - C(\vec{a},\vec{c}) = \sum_{\lambda=1}^{8}\left[P_\lambda A(\vec{a},\lambda)A(\vec{b},\lambda)\left(1 - A(\vec{b},\lambda)A(\vec{c},\lambda)\right)\right]. \tag{5}$$

From here, we can take the absolute value of both sides of the equation and use the triangle inequality to produce the fact that

$$|C(\vec{a},\vec{b}) - C(\vec{a},\vec{c})| \leq \sum_{\lambda=1}^{8}\left[|P_\lambda||A(\vec{a},\lambda)A(\vec{b},\lambda)||1 - A(\vec{b},\lambda)A(\vec{c},\lambda)|\right]. \tag{6}$$

However, certain facts can simplify this relation. Since probability is always non-negative, $|P_\lambda| = P_\lambda$, and since $A(\vec{a},\lambda)A(\vec{b},\lambda) = \pm 1$, $|A(\vec{a},\lambda)A(\vec{b},\lambda)| = 1$. Furthermore, the relation $1 - A(\vec{b},\lambda)A(\vec{c},\lambda)$ can equal either 2 or 0, but in either case, the result is greater than or equal to 0 and therefore, $|1 - A(\vec{b},\lambda)A(\vec{c},\lambda)| = 1 - A(\vec{b},\lambda)A(\vec{c},\lambda)$. These assumptions lead to the simplified relation that

$$|C(\vec{a},\vec{b}) - C(\vec{a},\vec{c})| \leq \sum_{\lambda=1}^{8}\left[P_\lambda\left(1 - A(\vec{b},\lambda)A(\vec{c},\lambda)\right)\right]. \tag{7}$$

Finally, we can distribute P_λ and split the summation to produce

$$|C(\vec{a},\vec{b}) - C(\vec{a},\vec{c})| \leq \sum_{\lambda=1}^{8}[P_\lambda] - \sum_{\lambda=1}^{8}\left[P_\lambda A(\vec{b},\lambda)A(\vec{c},\lambda)\right]. \tag{8}$$

Assuming normalized probability (i.e. $\sum_{\lambda=1}^{8}[P_\lambda] = 1$) and using our definition of correlation from equation (3), this finally leaves us with Bell's Inequality,

$$|C(\vec{a},\vec{b}) - C(\vec{a},\vec{c})| \leq 1 - C(\vec{b},\vec{c}). \tag{9}$$

Having directly derived this calculation from hidden variable assumptions, we know that all possible hidden variable theories must obey Bell's Inequality, so in order to disprove all hidden variable theories, one must experimentally find a violation of Bell's Inequality. Most physicists in the past have analyzed this relation as a purely mathematical one, but a graphical approach produces an interesting relation. By alternating the signs of the three correlations, we can produce four inequalities from our original one, and by associating $C(\vec{a},\vec{b})$ with the x-axis, $C(\vec{a},\vec{c})$ with the y-axis, and $C(\vec{b},\vec{c})$ with the z-axis to construct a "correlation-space," the intersection of these four inequalities form a tetrahedron, as seen in Figure 2.

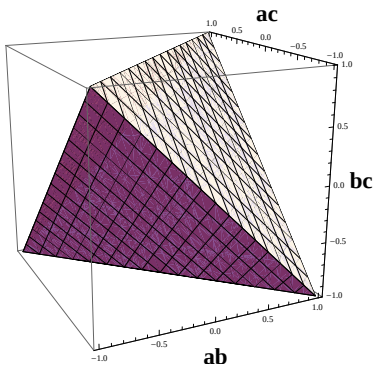

Figure 2: Tetrahedron representing all possible hidden variable correlations.

All possible correlation values in a hidden-variable context must lie within this tetrahedron and finding a violation of Bell's Inequality boils down to finding a point outside of this tetrahedron.

4 Experimental Application

In 1969, Clauser, Horne, Shimony, and Holt (CHSH) proposed an experimentally realistic version of Bell's Inequality[3] by introducing a fourth orientation, $\vec{b'}$, to estimate $C(\vec{b},\vec{c})$ using the relation that

$$C(\vec{b},\vec{c}) \geq C(\vec{b'},\vec{c}) + C(\vec{b'},\vec{b}) - 1. \tag{10}$$

Theoretically, we assumed that orientation $\vec{a}$ would produce the same result on either detector (i.e. $C(\vec{a},\vec{b}) = C(\vec{b},\vec{a})$), but in an experimental setting, this is unrealistic. The polarizer angle of 45° on one detector may not produce the exact same effect as 45° on the other. This relation and the fourth orientation associated with it enable us to isolate certain orientations to specific detectors: $\vec{a}$, $\vec{b'}$ to detector A, and $\vec{b}$, $\vec{c}$ to detector B. Originally, this estimation was used to create a purely mathematical relation of four orientations,

$$|C(\vec{a},\vec{b}) - C(\vec{a},\vec{c})| + C(\vec{b'},\vec{b}) + C(\vec{b'},\vec{c}) \leq 2, \tag{11}$$

but for the more intuitive graphical approach, we will use equation (10) to estimate $C(\vec{b},\vec{c})$ as our final z-component.

At the time of the initial introduction of Bell's Inequality and the CHSH inequality, optical technology was not advanced enough to establish a clear violation. However, as time passed and technology improved, conclusive experiments began to show up, notably that of Alain Aspect,[4] and in 2002, Dietrich Dehlinger and Morgan W. Mitchell performed one such experiment using correlated photons.[5] Our experimental work was based on their experimental set-up as follows.

Initially, 402 nm photons just within the visible blue range are produced by a diode laser. To ensure

uniform polarization and wavelength, the beam passes through a linear polarizer and a blue filter. A pair of lenses then collimates the beam into a small point and a rotatable quartz plate introduces a phase shift to the incoming light. Next, the photons pass through a pair of birefringent Beta-Barium-Borate (BBO) crystals to undergo what is known as spontaneous parametric down conversion. In this process, the input or "pump" photon is converted into two separate photons, the "signal" and "idler" photons. Each photon obtains half of the energy of the pump photon (804 nm wavelengths) and the polarization of both photons is perpendicular to that of the pump. In accordance with the conservation of momentum, our downconverted photons veer off at an angle of $\pm 3^\circ$ with relation to the original beam. At the end of these paths, photons are passed through red filters and focused onto two avalanche photo diodes (APD) to monitor coinciding detections of these photons, ensuring the consideration of only downconverted light. Furthermore, the optical paths are enclosed in a box of opaque material and measurements are taken in complete darkness. The output of the APD's is then passed through a wire delay and sent to a time-to-amplitude converter (TAC). A multichannel analyzer interprets the output of the TAC and finally displays a graph showing registered photon detections versus the time delay between the two detections. A noticeable peak should be located at the time of the wire delay and these detections can be counted as downconverted pairs.

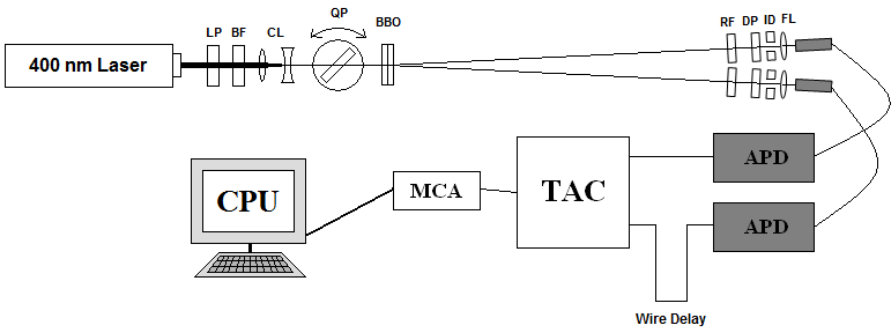

Figure 3: Theoretical diagram of experimental set-up. (LP=Laser Polarizer, BF=Blue Filter, CL=Collimating Lenses, QP=Quartz Plate, BBO=BBO Crystal, RF=Red Filter, DP=Detector Polarizer, ID=Iris Diaphragm, FL=Focusing Lens, APD=Avalanche Photodiode, TAC=Time-to-Amplitude Converter, MCA=Multichannel Analyzer, CPU=Desktop Computer)

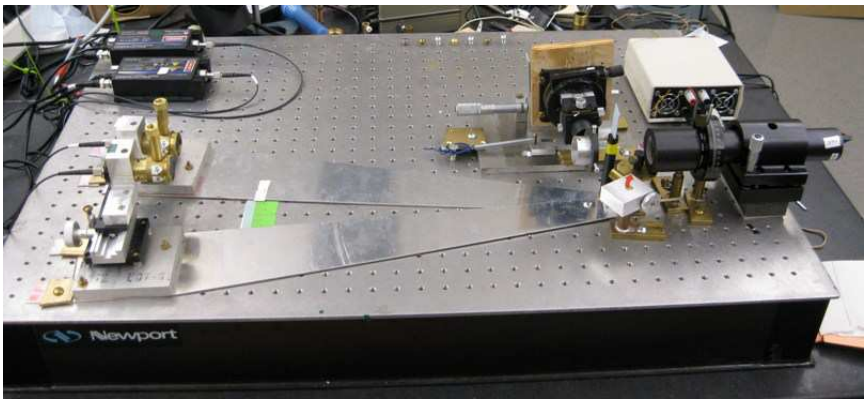

Figure 4: Actual experimental set-up. (Photograph by the author)

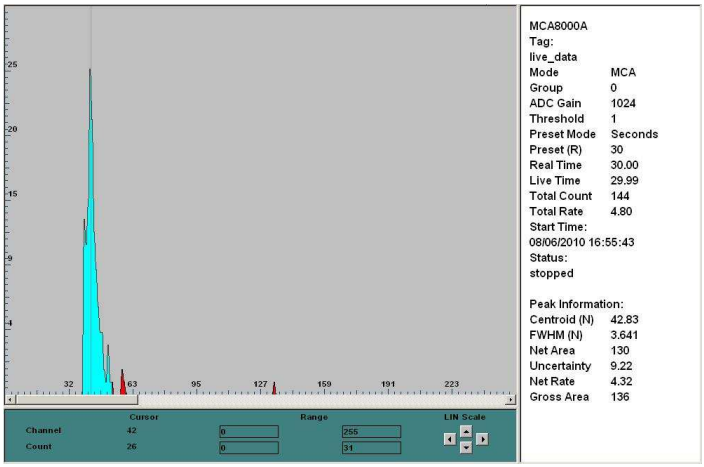

Figure 5: Sample TAC readout of photon pair detections versus the time delay between the two detections. As you can see, the greater percentage of coincidences occur in the general area of the time delay of the wire path. The units of the x-axis are the counting bins contained within the Time-to-Amplitude Converter (TAC) and are scaled based on the specific settings of the TAC.

To incorporate the abstract orientation, $\vec{a}$, from earlier theory, rotatable linear polarizers are placed in front of the detectors and the angles of these polarizers represent the orientation. Going back to our previous definition of correlation in equation (3), we noted that

$$C(\vec{a},\vec{b}) = \sum_{\lambda=1}^{8} \Big[P_\lambda A(\vec{a},\lambda) A(\vec{b},\lambda) \Big].$$

As mentioned earlier, $A(\vec{a},\lambda)A(\vec{b},\lambda)$ has two possible values: +1, corresponding to both photons passing through the polarizers and being detected or both being annihilated by the polarizers and not detected; and -1, corresponding to only one photon passing through its polarizer and being detected. In order to count non-detected pairs, we know that anything detected at an orientation orthogonal to $\vec{a}$ would not be detected using $\vec{a}$ itself. By this logic,

$$C(\vec{a},\vec{b}) = P_{ab} + P_{a_\perp b_\perp} - P_{ab_\perp} - P_{a_\perp b} \tag{12}$$

with $\vec{a}_\perp$ and $\vec{b}_\perp$ representing orientations orthogonal to $\vec{a}$ and $\vec{b}$ respectively, and P_{ab} representing the probability of detection using orientations $\vec{a}$ and $\vec{b}$. Since these orientations are the only possibilities, we can calculate the probabilities by dividing the amount of coincident detections using specific orientations by the total amount of coincidences, thus making the correlation measurement

$$C(\vec{a},\vec{b}) = \frac{N_{ab} + N_{a_\perp b_\perp} - N_{ab_\perp} - N_{a_\perp b}}{N_{ab} + N_{a_\perp b_\perp} + N_{ab_\perp} + N_{a_\perp b}}, \tag{13}$$

with N_{ab} being the number of photon coincidences detected using orientations $\vec{a}$ and $\vec{b}$.

With this experimental method in place, it is also necessary to optimize our laboratory equipment to generate the largest violation of Bell's Inequality. Firstly, the polarizer immediately after the laser must be adjusted so as to balance the coincidence counts using detector polarizer angles of 0°, 0° and 90°, 90°.

Theoretically, the orientation of the laser polarizer should be oriented somewhere close to 45°. Secondly, the quartz plate must be adjusted to counteract the birefringence of the BBO crystal so as to maximize the coincidence counts using detector polarizer angles of 45°, 45°. This orientation is more sensitive and may change depending on specific laboratory conditions such as the thickness of the quartz plate and BBO crystals.

5 Results and Conclusion

In order to produce the largest theoretical violation of Bell's Inequality, the four optimal detector polarizer orientations are $\vec{a} = -45°$, $\vec{b} = -22.5°$, $\vec{b'} = 0°$, and $\vec{c} = 22.5°$, as seen in Figure 5.

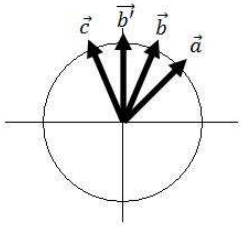

Figure 5: Optimal detector polarizer orientations ($\vec{a} = -45°$, $\vec{b} = -22.5°$, $\vec{b'} = 0°$, $\vec{c} = 22.5°$).

Using these orientations, the best calibrated run was able to produce correlations of $C(\vec{a}, \vec{b}) = 0.743$, $C(\vec{a}, \vec{c}) = -0.622$, $C(\vec{b'}, \vec{b}) = 0.622$, and $C(\vec{b'}, \vec{c}) = 0.742$. Typical runs did not deviate far from these values, but this optimal example best illustrates the suggested concept. Placing these values in the CHSH inequality of equation (11), one can observe a large violation in that

$$0.743 - (-0.622) + 0.622 + 0.742 = 2.729 \not\leq 2, \tag{14}$$

and with an experimental uncertainty of $\sigma = \pm 0.596$, this violates the inequality by an entire standard deviation. Furthermore, we can use equation (10) to approximate a value of $C(\vec{b}, \vec{c}) \geq 0.364$. Using these values in equation (9), Bell's Inequality itself is violated in that

$$|0.743 - (-0.622)| \not\leq 1 - 0.364 \quad \Rightarrow \quad 1.365 \not\leq 0.636, \tag{15}$$

but more importantly, if $C(\vec{a}, \vec{b})$, $C(\vec{a}, \vec{c})$, and $C(\vec{b}, \vec{c})$ are used as spatial coordinates in correlation space, the point plotted lies outside of the hidden-variable tetrahedron as seen in Figure 6.

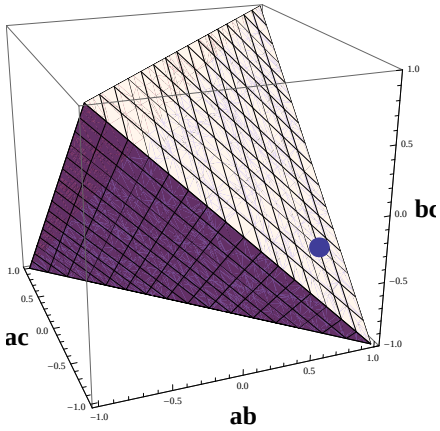

Figure 6: Graphical breach of Bell's Inequality, the set of correlations lies outside of the hidden-variable tetrahedron ($C(\vec{a},\vec{b}) = 0.743$, $C(\vec{a},\vec{c}) = -0.622$, and $C(\vec{b},\vec{c}) = 0.364$).

Having established these experimental violations, one can conclusively dismiss all hidden-variable theories as improper representations of nature due to their inability to predict every possible outcome. Where quantum mechanical interpretations escape this fate is in the fact that they do not necessarily have to abide by the assumption of locality. In theory, photons randomly choose a polarization based on the probability distribution dictated by their wavefunction, but only when they are measured at the detector polarizers. In order to maintain their identical polarization, they are somehow able to affect each other instantaneously even after gaining enough separation to negate locality, a perfect example of quantum entanglement. This "spooky action at a distance,"[6] as famously put by Einstein, would appear to violate causality, a crucial principle in the physical world, but the random nature of the effect disallows any form of communication, therefore preserving causality. While our experimental results do not explicitly confirm quantum mechanical interpretations themselves, it does reinforce them by eliminating the possibility of hidden variables.

Acknowledgments

A special thanks goes out to Alan Thorndike for his guidance in this project among many others throughout my undergraduate career. I would like to thank the University of Puget Sound, for initially sponsoring this research, as well as the many people who proofread this document. Finally, I would like to thank the Journal of Undergraduate Research in Physics for this opportunity and all of their help throughout this process.

References

[1] A. Einstein, B. Podolsky, and N. Rosen, *Can Quantum Mechanical Description of Physical Reality Be Considered Complete?* Phys. Rev. **47**, 777-780 (1935).

[2] J.S. Bell, *On the Einstein Podolsky Rosen Paradox*, Phys. (N.Y.) **1**, 195-200 (1964).

[3] J.F. Clauser, M.A. Horne, and A. Shimony, R.A. Holt, *Proposed Experiment to Test Local Hidden-Variable Theories*, Phys. Rev. Lett. **23** (15), 880-884 (1969).

[4] A. Aspect, P. Grangier, and G. Roger, *Experimental Tests of Realistic Local Theories via Bell's Theorem*, Phys. Rev. Lett. **47** (7), 460-463 (1981).

[5] D. Dehlinger and M.W. Mitchell, *Entangled Photons, Nonlocality, and Bell Inequalities in the Undergraduate Laboratory*, Am. J. Phys. **70** (9), 903-910 (2002).

[6] M. Born and A. Einstein, *The Born-Einstein Letters: The Correspondence Between Albert Einstein and Max and Hedwig Born, 1920-1955* (Walker, New York, 1971), pp. 157-160.

[7] J.S. Bell, *On the Problem of Hidden Variables in Quantum Mechanics*, Rev. Mod. Phys. **38** (3), 447-452 (1966).

[8] P.G. Kwiat, K. Mattle, H. Weinfurter, and A. Zeilinger, *New High-Intensity Source of Polarization-Entangled Photon Pairs*, Phys. Rev. Lett. **75** (24), 4337-4341 (1995).

Effects of Catalyst Components on Carbon Nanotubes Grown by Chemical Vapor Deposition

Tasha Adams*, Binh Duong**, and Supapan Seraphin**
*Department of Optical Engineering, Norfolk State University; **Department of Material Science and Engineering, University of Arizona
Integrated Optics for Undergraduates (IOU)
NSF-Sponsored Research Experience for Undergraduates (REU) Program

Abstract

In this paper, we study the role of each of the four chemical components of a catalyst system used in growing carbon nanotubes (CNTs). Our goal is to be able to grow desirable carbon nanotubes by chemical vapor deposition (CVD), which is believed to be the most practical growth method for CNTs. The catalyst used in our process is known for inducing Y-junction CNTs. To the best of our knowledge, there has not been a thorough investigation on the importance of each chemical component used during the CNT growth. To identify the impact that each component has on CNT growth, we prepared nine samples by either excluding or doubling the amount of each component (iron nitrate, aluminum oxide, and molybdenum). We used one of three different solvents including methanol, DI water, or ethanol for the catalyst solutions. We found that 1) all three catalyst components are needed in effective growth of CNTs; 2) molybdenum has a significant role in CNT growth and y-junctions in our system; 3) the solvent has noteworthy effect on the degree of CNT crystallinity of the nanotubes and 4) the growth of multiple samples at the same time may cause interaction from one sample to the next.

Key Words: Y-Junction, Iron Nitrate Nonahydrate, Aluminum Oxide, and Molybdenum Acetylacetonate

1. Introduction

For nearly twenty years, since their discovery, carbon nanotubes (CNTs) have been studied for their potential nanotechnology applications. These hollow structures are light weight, have varying optical and electrical characteristics, and are significantly stronger than all structural material currently used. However, the development of CNTs is a huge drawback in the utilization of carbon nanotubes in current technologies. Efficient and cost effective growth methods are the key to mass production of carbon nanotubes.[1]
In the prospects of achieving this goal, researchers across the world are working to understand and control the methods of CNT growth. Four basic parameters affect CNT growth in a chemical vapor deposition (CVD) system: pressure, temperature, gases, and the metal-support-interface (MSI). In our study, the flow rates of methane and hydrogen have been separately tested.[2] The

best flow rates for each gas has been observed and established as constants in this study. To further the examination of the impact of chemicals using the CVD method to grow CNT, the catalyst in the metal-support-interface (MSI) is tested in this paper. The different components of the catalyst were altered in order to identify their importance in CNT growth and were compared to a control that followed the report by Kong et al. [3]

2. Experimental procedure

Growing carbon nanotubes requires MSI preparation and a controlled growth environment. In this experiment everything but the chemical ratio of the catalyst was kept consistent to investigate the importance each chemical component has in CNT production. Preparation of the catalyst system followed Kong et al. occurred in various steps: measuring, sonicating, dissolving, and curing. The control sample contained a combination of 30 mg of aluminum oxide, Al_2O_3; 40 mg of iron (III) nitrate nonahydrate, $Fe(NO_3)_3 \cdot 9H_2O$ and 10 mg of Molybdenyl acetylacetonate, $Mo(acac)_2$ in 30 ml of methanol. In the following nine samples, the amount of Al_2O_3, $Fe(NO_3)_3 \cdot 9H_2O$, or $Mo(acac)_2$ was altered one at a time by either removing or doubling a chemical component as shown in Table 1. We also investigated the effect of the solvent in the catalyst solution on the CNT growth by using methanol, DI water or ethanol.

We used two different ways of depositing the catalyst solution on the substrate. The first method required dropping the solution on the samples and letting it air dry (labeled "air"). By this method, as shown in Figure 1, everything appears crowded and it is hard to observe individual CNTs. The second method utilized the spin coater to deposit the solution. As seen in Figure 2 (labeled "spin"), this method induces cleaner images. It is for this reason that spin coating proves to be the better method to use for our purpose. With it we can individually observe CNTs to see the effects of changing our experimental parameters. Based on those grounds, we chose images from the second method for most of this paper.

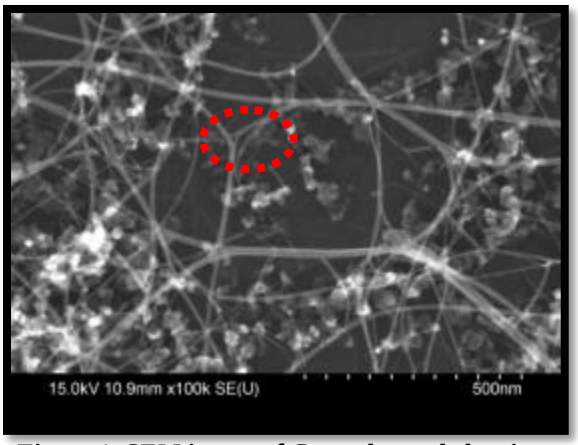

Figure 1. SEM image of Control sample by air drying (air). Red circle indicates y-junction.

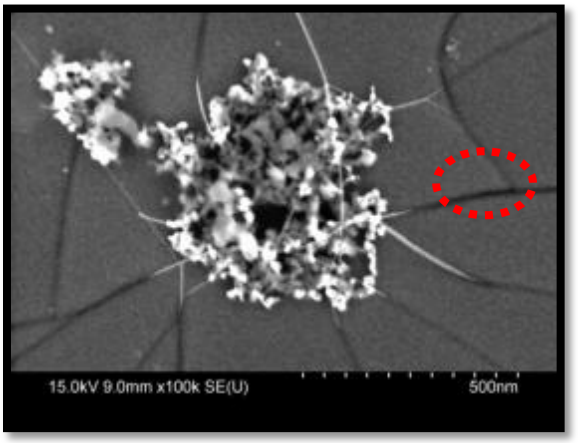

Figure 2. SEM image of control sample after spin coating (spin). Red circle indicates y-junction.

Preparation of the samples by the "air" method took many steps. After measuring and combining the solution, the samples were sonicated for one to two hours. Immediately after sonication, the samples were added by droppers to the silicon substrate and cured at 150°C to

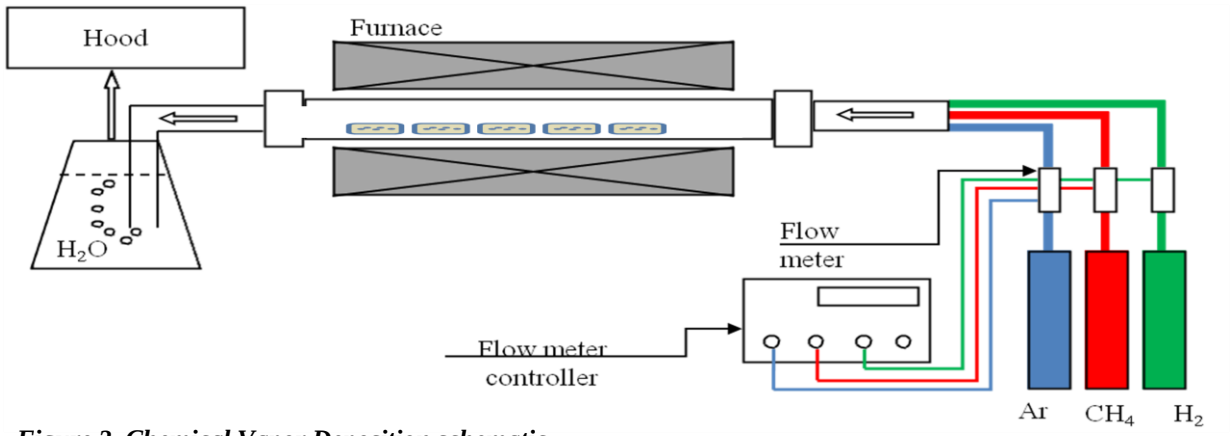

Figure 3. Chemical Vapor Deposition schematic.

Samples											
		Control	B	C	D	E	F	G	I	J	K
Component	Aluminum Oxide (mg)	30		60							
	Iron (III) Nitrate Nonahydrate (mg)	40				80					
	Molybdenyl acetylacetonate (mg)	10						20			
	Solvent Methanol or other (ml)	30							60	DI water	Ethanol

Table 1. Table of samples used in the experiment. The control sample uses the established formula provided by Kong et al.

evaporate the solvent. With the MSI prepared the samples were ready for CNT growth. The samples were inserted into the one inch quartz tube furnace as is seen in the diagram from Figure 3. The flow rates for our system gases were 240 cc/min for Hydrogen, H_2; 730 cc/min for Argon, Ar; and 600 cc/min for methane, CH_4. During preheating the tube was kept cool by Ar as the temperature of the furnace reached 900°C. Once at the growth temperature, the Ar gas flow was replaced with methane and H_2 gas.

The CH_4 was used for the carbon source and the H_2 was used to prevent the growth of amorphous carbons on the samples.[4] After 15 minutes the furnace was turned off and the gases were once again replaced with Ar to prevent the CNTs from burning in the heat. Samples were characterized by using Field-emission scanning electron microscopy (FESEM) S-4800 and transmission electron microscopy (TEM) for morphology and internal structure analysis and the state-of-the-art SEM-Renishaw Raman system for optical characterization.

3 | Effect of Catalyst

3. Results and discussion

Control Sample

Our catalyst produced y-junctions. While the CNTs grew in our system they formed in all directions and overlap each other. It is suggested that molybdenum may play a critical role in the growth of the y-junction.[5] Figure 4 is a TEM image showing bundles of single-walled CNTs. The diameter of tubes is in the range of 1-2 nm.

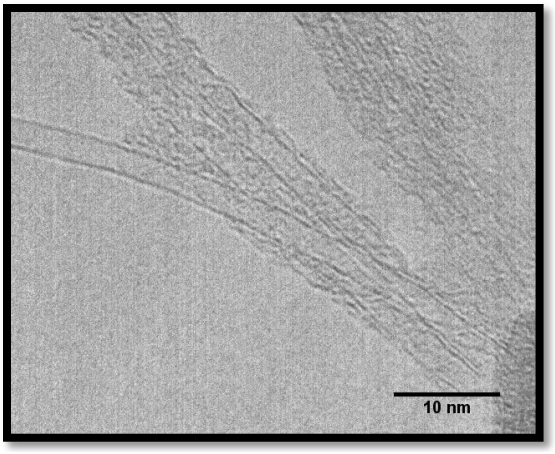

Figure 4. TEM image of control

We also analyzed the CNTs using Raman Spectroscopy technique. The Raman uses a beam of light to excite the sample material. The wavelength of the laser is 514 nm with a beam diameter of ~ 1 μm. A typical Raman spectrum of CNTs is shown in Figure 5. It contains important information about CNTs including scattering at G-band, D-band, RBM, and G'-band.[6,7] The G-band stands for the graphitic band and is the peak found around 1590cm^{-1}. It corresponds to the vibration of carbon bonds in the graphitic planes. The D-band is better known as the defect-band, occurring around the range of 1350 cm^{-1}, and contains information about the defects in the graphitic structure. The ratio of D/G is used to define the degree of crystallinity. When this value is below 0.02, it shows low defect in the sampled CNTs. The RBM (Radial Breathing Mode), which occurs in the 120-250cm^{-1} range, contains information about the diameter of the CNTs. The peak marked by an asterisk (*) at 500 cm^{-1} on the Raman of the sample shown in Figure 6 was the signal from the substrate and can be ignored during analysis.

The control sample set the base line for our research. TEM analysis was also used to confirm the formation of CNTs. We found that the CNTs in the control sample have an average diameter of 1.35nm. The average degree of crystallinity (ratio of D/G) of our control was 3.41 (an average from two Raman Spectra).

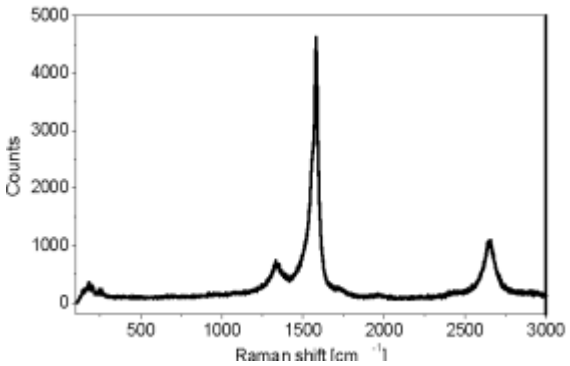

Figure 5. Typical Raman spectrum for a CNT sample

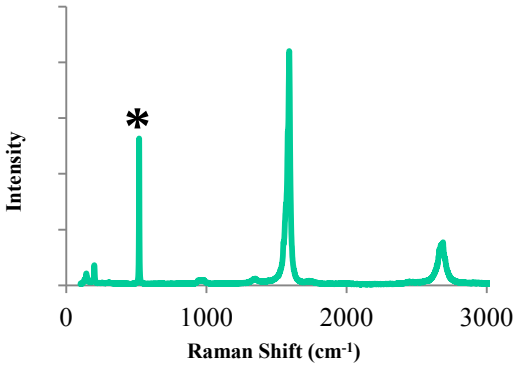

Figure 6. Raman spectrum of control sample. The * marks where the silicon MSI is responding to the Raman excitement.

Effect of Catalyst Component

Methane, as the most kinetically stable hydrocarbon, is an ideal carbon feedstock for decomposition to form CNTs. It does not naturally decompose at 900ºC. The interaction between the catalyst and methane is responsible for the feedstock's decomposition into carbon. This is an important concept to understand when characterizing the following samples. It has been found that in the presence of molybdenum, methane will decompose into hydrogen and carbon. The presences of catalyst in a growth environment similar to ours can help alkaline gases such as propane, ethane and methane decompose at 400°C -500°C lower than their self-pyrolysis temperature. The catalyst used in our system is an alloy and is composed of both iron and molybdenum which offers both thermodynamic and chemical benefits. [8]

In the absence of a catalyst component, CNT growth did not occur as shown in SEM image of Figure 7.

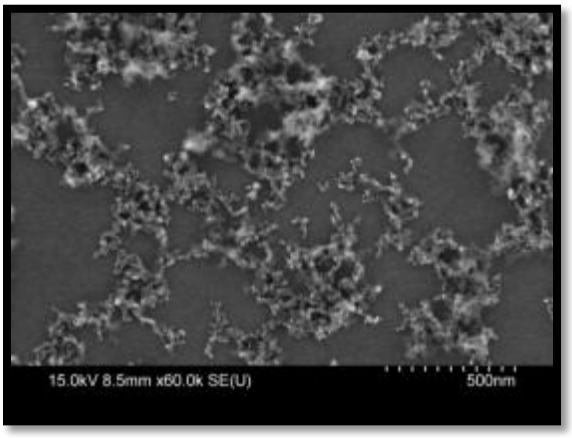

Figure 7. SEM image of no Moybdenyl Acetylacetonate. (air)

In the case of the samples with no Al_2O_3, there were scarce amount of CNT in the first round and there was no growth in the second round. With the omission of $Fe(NO_3)_3 \cdot 9H_2O$ both rounds did not grow CNTs. Due to the removal of $Mo(acac)_2$ in the first round the CNT growth followed the trend of no growth, but the second round of growth produced few CNTs without the y-junctions, as shown Figure 8.

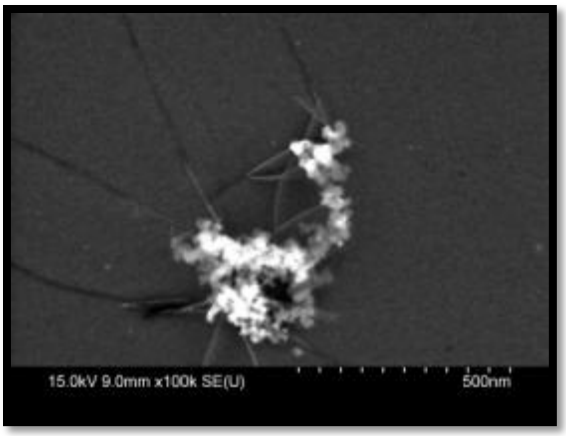

Figure 8. SEM image of 2nd round of no Moybdenyl Acetylacetonate. (spin)

The inconsistency of the results between two rounds of experiments may be due to the fact that we put five samples at a time into the experimental setup. This possibly resulted in cross interaction from sample to sample in the furnace when growing CNTs. Excess carbon that was produced by one sample could have contaminated the samples that followed it in the quarts tube. Unfortunately, there was no order that we placed the samples in during the two rounds of experiments so it is unknown what samples interacted with each other and the impact that it had.

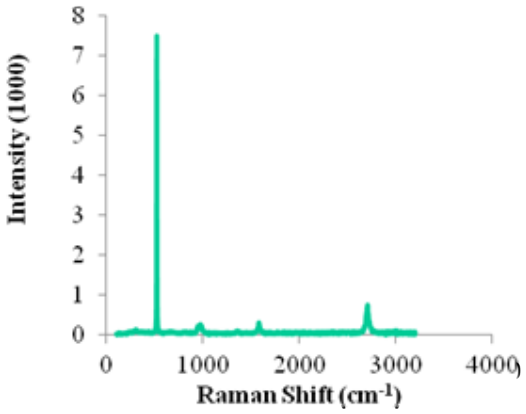

Figure 9. Raman Spectrum of no Aluminum oxide.

Even though SEM images do not show presence of CNTs on the samples without Aluminum oxide, Raman spectrum contains characteristic peaks of CNTs as shown in Figure 9.

Effect of Catalyst Concentration

We found that the sample with double iron nitrate contains higher CNTs density as shown in Figure 10. This is expected since the methanol solvent has a higher saturation with the addition of a catalyst component. There is no information collected on weight to compare samples before and after growth. Therefore, it is inconclusive if any of the three chemical components had more of an impact on CNT growth than the others.

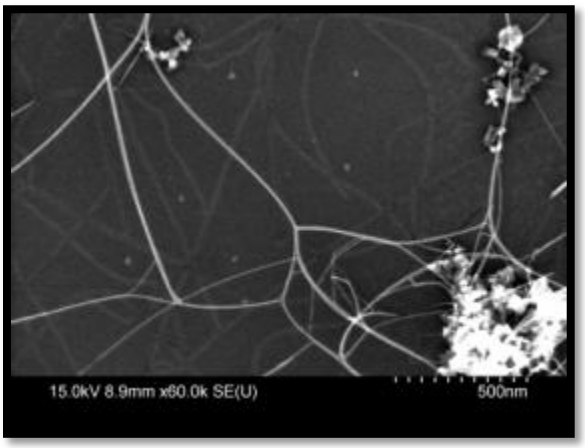

Figure 10. SEM image of double Iron Nitrate. (spin)

Effect of Solvent

When compared with the Figure 1, the samples of DI water (Figure 11) and ethanol (Figure 12) appears to have less CNT growth. Other than SEM images this cannot be confirmed. Once again weighing the samples could provide more information. This is a suggestion for future study.

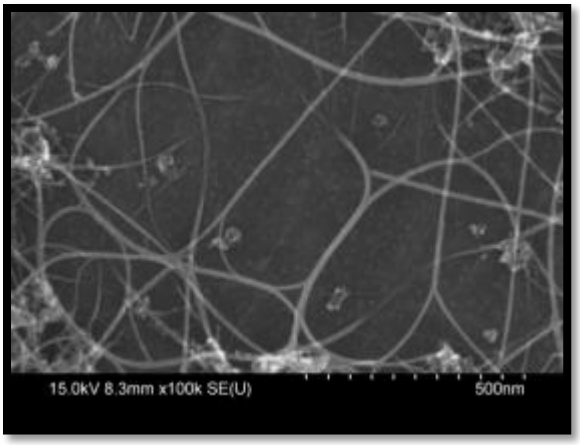

Figure 11. SEM image of DI water. (air)

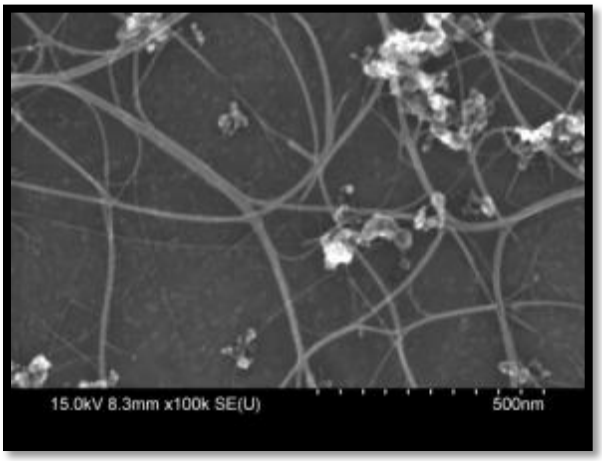

Figure 12. SEM image of no Ethanol. (air)

Raman results show a small but noteworthy effect on the average degree of crystallinity of the CNTs grown with the DI water (.0528) and ethanol (0.0566) samples. The degree of crystallinity for the control sample of methanol (0.0341) was slightly lower. This is an interesting observation because it is believed that the solvent evaporated before CNT growth. However, if in further studies this small trend continues then detailed investigation of the solvent effect on CNT growth should be carried out.

It should be noted that there was no noticeable variation on CNT diameters. There were highly intense peaks of Raman spectra found in these samples for particular diameter, but we found no significant differences between samples. As it stands

more studies need to be performed to come to any conclusions on the solvents impact.

Additional Findings Discussion

The role of each chemical component is discussed as follows. In the case of iron, it produces the best quality tip-growth[9, 10] CNTs (from Raman results) through "carbon dissolution precipitation mechanism." Iron is the medium that the carbon diffuses through to form CNTs. Diffusion is more thermodynamically favorable than carbide formation for iron. On the other hand, molybdenum is a "carbide formation decomposition" element and traditionally produces CNTs by the base-growth mechanism.[11] Contrasting iron, molybdenum carbide is more thermodynamically favorable than carbon diffusion at our working temperatures, but in conditions of 1200°C carbon diffusion is more favorable.[12] Aluminum oxide is believed to promote the degree of crystallinity. However, the optimization varies from one catalyst system to another. [4]

4. Conclusions

From this experiment we reach several conclusions as follows. The most important observation is that all three catalyst components are needed in effective growth of CNTs based on the fact that the omission of a catalytic component resulted in no CNT grow. Secondly, we can conclude that molybdenum has a significant role in CNT growth and y-junctions in our system. Third, we found that the solvent has a significant effect on degree of crystallinity in our system. Finally, we learned that growing multiple samples of CNTs with varying compositions at the same time may cause interaction from one sample to the next. This added complications in our attempt to interpret results.

5. Future Work

In future works we will repeat the sample growths in this experiment by growing each sample independently to create a more controlled environment. We will weigh the samples before and after CNT growth. This will help provide more information when altering the catalyst concentration, and perhaps provide more insight on the impact each component has on CNT growth.

In addition we will continue to investigate the solvents impact on CNT growth and their degree of crystallinity. It would also be beneficial to understand how the catalyst breaks down during the different stages of preparation.

Lastly, it would be important to identify the gasses produced by catalyst and methane interaction in our CVD system. If we could understand what output gases are being created perhaps a catalyst ration of the three components could be established to use all the carbon produced by the catalytic methane decomposition.

6. Acknowledgements:

This research was supported by the National Science Foundation through an REU Site under grant #EEC-1004331, the University Spectroscopy and Imaging Facilities (USIF) at The University of Arizona, and the Center for Integrated Access Networks- Integrated Optics for Undergraduates (CIAN-IOU). Special thanks are given to Phil Anderson (TEM operator).

7. References

1. C. Oncel, Y. Yurum. Carbon Nanotube Synthesis via the Catalytic CVD Method: A Review on the Effect of Reaction Parameters. Fullerenes, Nanotubes, and Carbon Nanostructures, 14 (2006): 17–37.
2. B. Duong, Y. Peng, M. Ellis, S.Seraphin, H. Xin. Combined Raman Spectroscopy and SEM Analysis of Chemical Vapor Deposition Grown Carbon Nanotubes. Microscopy Society of America and the Microbeam Analysis Society annual conference. (2008) Poster.
3. J. Kong, H. T. Soh, A. M. Cassell, C. F. Quate, H. Dai. Synthesis of individual singlewalled carbon nanotubes on patterned siliconwafers. Nature 395. (1998) : 878 -881.
4. A. R. Harutyunyan, B. K. Pradhan, U. J. Kim, G.Chen, and P. C. Eklund. CVD Synthesis of Single Wall Carbon Nanotubes under "Soft" Conditions. Nano Letters 2.5 (2002): 525-530.
5. Y. C. Choi, W. Choi. Synthesis of Y-junction single-walled carbon nanotubes. Carbon. 43 (2005): 2737-41.
6. A. Jorio, M. A. Pimenta, A. G. Souza Filho, R. Saito, G. Dresselhaus and M. S. Dresselhaus. Characterizing carbon nanotube samples with resonance Raman scattering New Journal of Physics 5 (2003) 139.1–139.17
7. S.Costa, E. Borowiak-Pale, M. Krusznynska, A. Bachmatiuk, R. J. Kalenczuk. Characterization of carbon nanotubes by Raman spectroscopy. Mater Sci-Poland 26.2 (2008): 433-441.
8. G. P. Huffman, N. Shah, Y. Wang, F. E. Huggins. Catalytic Dehydrogenation of Hydrocarbons: Alternative, One Step Process to Produce Pure Hydrogen and Carbon Nanotube Byproducts. Prepr. Pap.-Am. Chem. Soc., Div. Fuel Chem 49.2 (2004): 731-732.
9. J. Kong, A. M. Cassell, H. Dai. Chemical vapor deposition of methane of single-walled carbon nanotubes. Chem. Phys. Lett. 292 (1998): 567-74.
10. S.P. Chai, S.H.S. Zein, and A.R. Mohamed, A Review On Carbon Nanotubes Production Via Catalytic Methane Decomposition. In: 1st National Postgraduate Colloquim NAPCOL (2004).
11. S. Curtarolo, N. Awasthi, W. Setyawan, A. Jiang, K. Bolton, T. Tokune, and A. R. Harutyunyan. Influence of Mo on the Fe:Mo:C nano-catalyst thermodynamics for single-walled carbon nanotube growth, Phys. Rev. B 78.5 (2008).
12. H.J. Dai, A.G. Rinzler, P. Nikolaev, A. Thess, D.T. Colbert, R.E. Smalley. Single-wall nanotubes produced by metal-catalyzed disproportionation of carbon monoxide. Chem. Phys. Lett. 260 (1996): 471-475

SDSS-II: DETERMINATION OF SHAPE AND COLOR PARAMETER COEFFICIENTS FOR SALT-II FIT MODEL

L. Dojcsak,[1] J. Marriner [2]

December 4, 2011

ABSTRACT

In this study we look at the SALT-II model of Type IA supernova analysis, which determines the distance moduli based on the known absolute standard candle magnitude of the Type IA supernovae. We take a look at the determination of the shape and color parameter coefficients, α and β respectively, in the SALT-II model with the intrinsic error that is determined from the data. Using the SNANA software package provided for the analysis of Type IA supernovae, we use a standard Monte Carlo simulation to generate data with known parameters to use as a tool for analyzing the trends in the model based on certain assumptions about the intrinsic error. In order to find the best standard candle model, we try to minimize the residuals on the Hubble diagram by calculating the correct shape and color parameter coefficients. We can estimate the magnitude of the intrinsic errors required to obtain results with χ^2/degree of freedom = 1. We can use the simulation to estimate the amount of color smearing as indicated by the data for our model. We find that the color smearing model works as a general estimate of the color smearing, and that we are able to use the RMS distribution in the variables as one method of estimating the correct intrinsic errors needed by the data to obtain the correct results for α and β. We then apply the resultant intrinsic error matrix to the real data and show our results.

INTRODUCTION

In an effort to expand upon the already vast Sloan Digital Sky Survey (SDSS) –which imaged more than 8000 square degrees of the sky from 2000 to 2005 using the 2.5 meter telescope (Gunn et al. 2006) at the Apache Point Observatory (APO) in New Mexico– the SDSS-II Supernova Survey (Frieman et al. 2008) was undertaken to detect and measure the light curves for Type IA supernovae (SNe) to study supernova (SN) properties and to use them to measure the expansion of the universe. The CCD camera (Gunn et al. 1998) of the SDSS telescope obtains images in five optical passbands, or filters, of *ugriz* (Fukugita et al. 1996), standard ranges of wavelengths, which are then processed by the PHOTO photometric reduction pipeline (Lupton et al. 2001; Ivezi´c et al. 2004). Previously taken co-added images (Sako et. al 2008) are subtracted from the new images in order to correctly identify Type IA supernovae.

Type IA supernovae, colossal explosions of white dwarf stars, are just one subcategory of SNe. These white dwarves are believed to explode by undergoing a thermonuclear reaction caused by accumulating mass from a binary companion star and exceeding the Chandrasekhar limit, causing an explosion that is more luminous than a galaxy. These supernovae are studied because they have a narrow range of absolute magnitudes that are well known. In addition, they have distinctive spectra due to the conditions under which the dwarf stars become supernovae that lack Hydrogen and produce heavier elements such as Sulfur and Silicon. Since the absolute magnitude of an SN IA is known, the apparent magnitudes in this and other surveys are used to determine the distances to the SNe. The supernovae received rapid spectroscopic follow-up by supplementary telescopes in order to determine redshift and to make sure data was restricted to high-quality SN candidates for analyses. An additional benefit of SDSS-II was to complement other surveys of this type by providing data between the low and high redshift ranges, where Type IA SNe had not been observed before.

Over the course of three fall seasons (September 1 – November 30) in 2005, 2006, and 2007, the SDSS-II SN Survey (Frieman et al. 2008) did repeat imaging of a 300 square degree equatorial stripe, 2.5 degrees wide, in the Southern Galactic hemisphere, designated as SDSS stripe 82 (Kessler et. al 2009a). The survey discovered and obtained data on approximately 500 Type IA SNe in the 0.05-0.40 redshift range in order to study the accelerating cosmic expansion as well as to improve the statistical scatter about the Hubble fit diagram, which plots the distance of cosmological objects as a function of redshift.

In order to measure the light curve of each SN from the survey, we chose to apply the Spectral Adaptive Light Curve Template Fitting (SALT-II) (Guy et al. 2007) model in this research as presented in the Supernova Analysis (SNANA) (Kessler et. al 2009b) software package for the SDSS. This fitting method uses a two-parameter model of light curve shape (x_1) and excess color (c) in order to compare it to a well measured SN with known parameters. The SALT-II fitter uses the following base equation for the absolute magnitude (M_b) of the SNe:

$$M_b = m_b - \mu(z) + \alpha x_1 + \beta c. \quad (1)$$

The equation shows the correlation between the absolute standard candle magnitude (M_b) to be proportional to the apparent magnitude that we measure in the B band (m_b), the distance modulus ($\mu(z)$), the shape of the light curve (x_1), which is a result of the location of its peak, and the excess color

[1] Lawrence Technological University, 21000 West Ten Mile Road, Southfield, MI 48075-1058
[2] Center for Particle Astrophysics, Fermi National Accelerator Laboratory, P.O. Box 500, Batavia, IL 60510

offset in the light curve (c). The parameters x_1 and c do not have any particular physical significance in the model; they account for anything that may change the shape or color of the SN light curves. We define the color offset as this particular change in the SN light curve color due to some unspecified factor such as redshift. The model for the absolute standard candle magnitude depends linearly on these shape (x_1) and color (c) parameters. The coefficients are α for the shape parameter (x_1) and β for the color parameter (c). Our purpose in this research is to observe trends in the results, by altering the intrinsic error model, and to try to calculate the correct α and β coefficients for use in determining the absolute magnitude (M_b) and the distance moduli (μ(z)). The intrinsic error model is an attempt to represent the intrinsic, or inherent, errors which we observe in the real data due to any number of unknown factors such as redshift, dust, or otherwise. We cannot yet account for this error due to known measurement error and therefore it does not appear in our simulations, but we observe it in the real data.

Before applying the model to the real data, we test it with a Monte Carlo simulation of SN light curves, provided in the SNANA package. The program SALT2mu is what we use to calculate the α and β parameter coefficients. Since we generate the Monte Carlo simulation with known values of α and β, we are able to test the program on how well it is able to calculate the shape (α) and excess color (β) coefficients. Thus, we can say with certainty that the correct values in the simulation are distributed about α = 0.11 and β = 2.60. We use this method to determine trends in altering specific parameters in the program SALT2mu as well as to improve the calculations on the α and β parameter for this type of analysis. We do this in order to find the best standard candle model by minimizing the residuals in the Hubble diagram.

SALT2mu ANALYSIS

We use the program SALT2mu, provided with the SNANA software package, in order to calculate the α and β coefficient values in both simulation and SDSS data. We adjust the intrinsic error to obtain χ^2 per degree of freedom equal to 1 (χ^2/DOF = 1) for good statistical results. χ^2 is determined by the following equation in the SALT2mu program:

$$\chi^2 = \sum_{i=1}^{N} \left[\frac{m_{bi} - m_0(z_i) - \mu(z_i) + \alpha x_{1i} - \beta c_i}{\sigma_i} \right]^2 . \quad (2)$$

The value of σ_i is equal to the measurement error in the numerator for the i^{th} supernova for all N supernovae, plus an intrinsic error that we do not fully understand. The intrinsic error itself is the additional error that we find in the real data, but not in the simulation, so we test for the correct values of this error by adding it to the total error (σ_i^2) in the simulation using a covariance error matrix to represent this intrinsic error for the total errors in m_b, x_1, and c, where the elements of the total error matrix are described by:

$$\sigma_i^2 = C_{11} + \alpha^2 C_{22} + \beta^2 C_{33} + 2\alpha C_{12} - 2\beta C_{13} - 2\alpha\beta C_{23}. \quad (3)$$

This total error is divided into parameters where $C_{ab} = C_{ab}^{meas.} + C_{ab}^{int.}$ and the program makes use of altering:

$$\Sigma_1 = \sqrt{C_{11}^{int.}} \equiv intrinsic\ error\ for\ m_b, \quad (4)$$

$$\Sigma_2 = \sqrt{C_{22}^{int.}} \equiv intrinsic\ error\ for\ x_1, \quad (5)$$

$$\Sigma_3 = \sqrt{C_{33}^{int.}} \equiv intrinsic\ error\ for\ c. \quad (6)$$

The subscripts (ab) define the specific elements of the covariance error matrix. The covariance error matrix is a method for adding in the intrinsic error, described by equations 4, 5, and 6. These are arbitrary values which we vary in order to test for the correct intrinsic error in our model that produces an output of χ^2 per degree of freedom equal to 1. Since we do not understand the source(s) of the intrinsic error, we want to know what happens to resultant values of α and β if we place the error completely in one intrinsic error. This paper examines the dependence on the assumed cosmological parameters and how the intrinsic error matrix has an effect on the outcome, including a possible solution using the color smearing model in SNANA.

Before we can attempt to test varying the intrinsic error matrix, we must restrict the equation so that the results do not vary based on assumptions about the cosmology. The SALT2mu program is written so that it can calculate the distance moduli for Type IA SNe by separating the determination of the shape and color parameter coefficients, α and β, from the determination of the cosmological parameters. We do not want the cosmology to have an effect on the determination of the α and β coefficients since we want to observe effects only due to the error. In order to do this, we split the data into equally ranged redshift bins for z = 0.02-0.42. By splitting the data into multiple bins, we create new M_b variables in the equation for each bin, thus minimizing the effect of the distance modulus, which is a function of the cosmological parameters.

In order to test the number of redshift bins that we would need, we use a standard SNANA Monte Carlo simulation with the SALT2mu program and use three different assumptions for the cosmological parameters:

$\Omega_\lambda \equiv$ Percent of Universe Made Up of Dark Energy,
$\Omega_K \equiv$ Curvature of the Universe,
w ≡ Pressure/Density Parameter at z=0.

First we assume the standard observed cosmological parameters where Ω_λ = 0.7, Ω_K = 0.0, and w = -1.0. These are the parameters we use in all other runs of the program with the standard simulation. The other two assumed cosmologies are Ω_λ = 0.0, Ω_K = 0.7, w = -1.0 and Ω_λ = 0.7, Ω_K = 0.0, w = 0.0. By increasing the number of bins from 1 to 19, we observe in Figures 1 and 2 that the values of α and β begin to converge when bins ≈ 4.

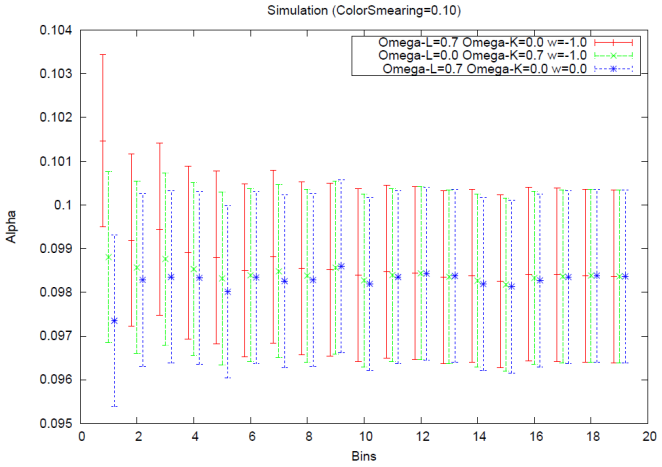

Figure 1 – Plot of α vs. number of redshift bins with error bars for three different assumed cosmologies.

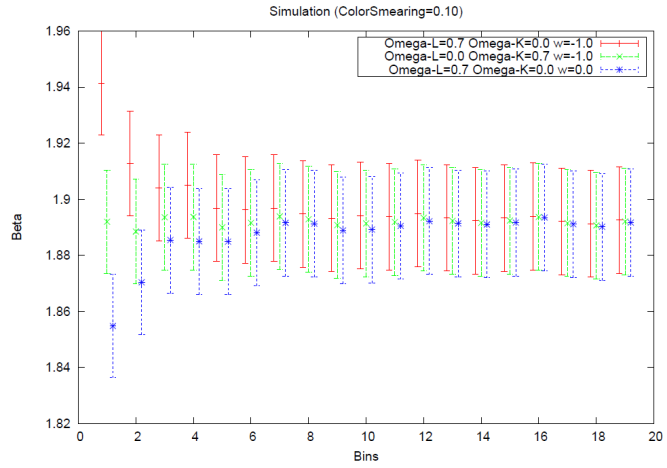

Figure 2 – Plot of β vs. number of redshift bins with error bars for three different assumed cosmologies.

The plots demonstrate that both α and β begin to converge after a low number of bins even for a simulation of 5000 SNe and that the results for the two parameters can be found independently of the cosmology parameters entered into the program. In theory, this could be performed for any size data with increasing bins, so long as it stays within the limits of the program of at least 5 entries per bin. However, this would become impractical as it would greatly increase computation time without producing significantly better results. The plots show that 4 bins are enough for further tests.

INTRINSIC ERROR MATRIX

Since we have determined that the α and β parameters can be found independent of the cosmology parameters with the use of multiple bins, we want to examine the trends caused by the intrinsic error matrix in the SALT2mu program. Assuming, in turn, that the intrinsic error for m_b, x_1, or c is increased from 0 in order to see how the results of the α and β coefficients are affected, we see that when Σ_1 is increased, α and β both decrease. When the intrinsic error in Σ_2 is increased, α increases and β decreases, and when the intrinsic error in Σ_3 is increased, α decreases and β increases. Increasing any individual intrinsic error also decreases the χ^2/DOF. However, the assumptions for the values of the intrinsic errors of m_b, x_1, and c are not compatible, as the results actually depend on the intrinsic error matrix.

Next, we want to find the intrinsic errors that would be needed if the errors were completely in m_b, x_1, or c. The method we used was to adjust the values of Σ_1 Σ_2 and Σ_3 independently in the program until we obtained a χ^2/DOF = 1 as shown in Tables 1, 2 and 3. Table 1 lists the results for the α and β value calculations for the standard SNANA Monte Carlo simulation. The exception is the first row of each table which lists the results of setting all three intrinsic errors to 0. It can be inferred from these results, that some sort of intrinsic error is needed, since setting the error matrix to 0 gives us a very high χ^2 value and therefore a χ^2/DOF that is much higher than 1.

TABLE 1 Standard SNANA Simulation

Intrinsic Error	χ^2	α	$\Delta\alpha$	β	$\Delta\beta$
Σ_1=Σ_2=Σ_3=0	17468	0.1510	0.00126	2.016	0.0103
Σ_1=0.1275	4319	0.1008	0.00186	1.910	0.0177
Σ_2=0.8792	4318	0.2069	0.00377	1.812	0.0257
Σ_3=0.05927	4318	0.0950	0.00209	2.424	0.0223

Table 1 – (4324 entries of 5000) The above table lists the values of α and β for the χ^2/DOF = 1 output with errors ($\Delta\alpha$ and $\Delta\beta$), with the exception of the first row, where all three intrinsic errors are set to 0.

We were not necessarily expecting to obtain the correct results for α and β with these assumptions for the intrinsic errors. What we might hope to see here is a distribution of results around the correct values of α = 0.11 and β = 2.60. However, we never quite get a value above 2.60 for β in the simulation. Although it would seem intuitive to simply increase Σ_3 in order to check that we are able to get a value of β = 2.60 due to the general trends, this does not attain the result that we seek since the values of α and β both converge towards an asymptote when one of the Σ values is increased infinitely.

Since this result relies on using the intrinsic errors in the diagonal of the error matrix only, another test of the program is to see if the correct values for α and β can be recovered by setting the correlation coefficients for the off-diagonal values between mb and x1, mb and c, and x1 and c to be some arbitrary value, since we do not know the correlation. Then we can alter the non-diagonal intrinsic errors in the error matrix to see if we can find a value which can recover β = 2.60 for any values, and α = 0.11 and β = 2.60 at the same time. The results show that it is possible. One example that we find is when Σ_1 = 0.1325 Σ_2 = 0.0 Σ_3 = 0.07 and with the m_b and c correlation coefficient equal to 0.9, the results we obtain are α = 0.109 and β = 2.60. However, this does not produce a χ^2/DOF = 1. Instead the value is closer to 2.

Another way to verify that the correct values of α and β can be recovered from the data can be done by using an

additional simulation in SALT2mu. The program is written with an internal simulation that can generate new values for the parameters m_b, x_1, and c from the Monte Carlo simulation that it then uses in the calculations. The results of the internal simulation are listed in Table 2 for the same SNANA Monte Carlo simulated data as before. These results verify that we can recover the correct α and β values with statistical accuracy.

TABLE 2 SALT2mu Internal Simulation with Stand. Simulation

Intrinsic Error	χ^2	α	$\Delta\alpha$	β	$\Delta\beta$
Σ_1=Σ_2=Σ_3=0	4210	0.1090	0.00096	2.620	0.0107
Σ_1=0.1275	4293	0.1084	0.00187	2.593	0.0228
Σ_2=0.8792	4268	0.1091	0.00157	2.630	0.0192
Σ_3=0.05927	4152	0.1119	0.00216	2.626	0.0270

Table 2 – (4325 entries of 5000) This table lists the values of α and β for the χ^2/DOF = 1 output with new generated values for m_b, x_1, and c by the program's internal simulation.

Finally we run the program for the real supernova data from SDSS-II without the internal simulation in order to observe the accuracy of our model. The results we obtain for α and β, shown in Table 3, are actually much higher in general than the ones we get from the Monte Carlo simulation. Thus, we can conclude that the intrinsic error values we are entering for the simulation and in the calculation are too low.

TABLE 3 SDSS-II 2005, 2006, 2007 Data

Intrinsic Error	χ^2	α	$\Delta\alpha$	β	$\Delta\beta$
Σ_1=Σ_2=Σ_3=0	1316	0.1857	0.00619	2.826	0.0477
Σ_1=0.146	344	0.1400	0.00970	2.655	0.0779
Σ_2=0.72	345	0.2922	0.01975	2.362	0.1157
Σ_3=0.05	344	0.1223	0.01100	3.227	0.1020

Table 3 – (350 SNe) This tables shows the results for α and β by running the program on the real SDSS-II SN data.

ESTIMATING INTRINSIC ERRORS

Our goal is to improve the scattering on the Hubble fit diagram by calculating the shape (x_1) and color (c) parameter coefficients α and β, which are in turn used to find the distance moduli (μ(z)). Therefore, we must have a reliable way of estimating the intrinsic errors in the real data to improve our current simulation model. Although we observe the scatter in the Hubble diagram, we are not sure what causes the scatter, or what the form of the intrinsic error matrix should be. However, we are able to calculate the intrinsic errors in the context of the SNANA color smearing (CS) model. The scatter in the distance modulus (μ(z)) is defined (Kessler et al. 2009c) as the RMS of the difference between the fitted and the generated distance modulus. In the same way, we can use this definition to estimate possible intrinsic error to each shape, color, and light magnitude by taking the difference in each simulated and generated variable for the Monte Carlo simulation to find the total error. One step we take in order to determine the correct values for the intrinsic errors is by applying the correct "color smearing" that we observe in the data to the simulations and estimate the correct intrinsic error values from the RMS of the data. The "color smearing" introduces an independent magnitude fluctuation in each optical passband of *ugriz* with the fluctuation being the same for all epochs (Kessler et al. 2009c). Since we are using a 0.10 color in the simulations as default, we use a range of values around the default to test it. The results are shown in Figure 3, A-F.

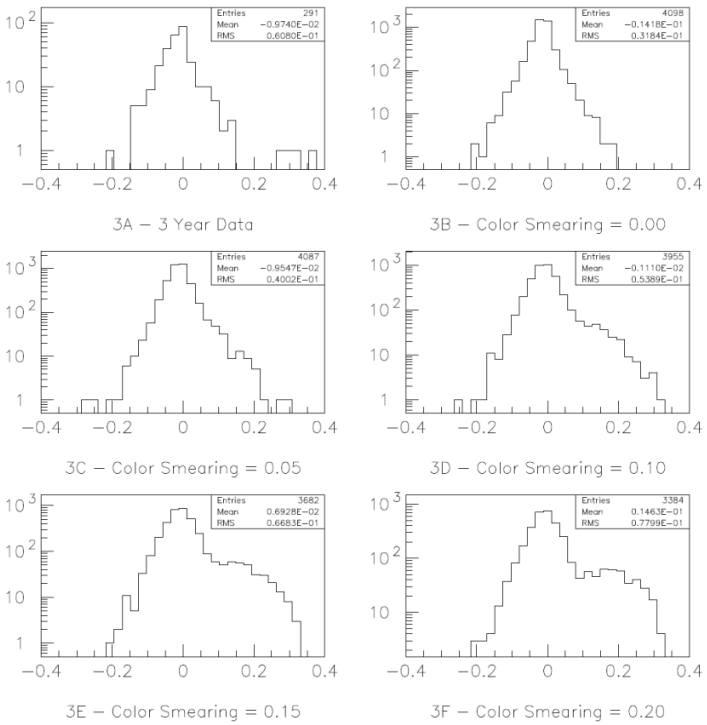

Figure 3A-3F – The above plots all show Δz = photometrically fit redshift – spectroscopically fit redshift (photoz – specz). Figure 3A shows the plot for Δz for the real data, and Figures 3B-3F show the plots for Δz for Monte Carlo simulations with color smearing 0.00, 0.05, 0.10, 0.15, and 0.20.

These plots show the RMS values for Δz, the difference of the photometrically and spectroscopically fit redshifts, which we assume to be very close to or the true value of the redshift (z). The RMS values in the distribution and the plots demonstrate that a 0.10 color smearing value is the closest to the real data. Although the distribution in the simulation is somewhat different from the real data, especially seen in the tail to the right of the zero, since the color smearing in the simulation is an ad hoc model designed to match the real data, we do not expect them to match exactly.

Therefore, we look at the results for the simulation with color smearing = 0.10 output of the Δ values for light magnitude (m_b), color (c), and shape (x_1) where Δ signifies that the distribution is the difference between the reconstructed value (from the light curve fit) and the true (simulated) value. These results are shown in Figure 4, A-C.

These plots indicate that according to the photometrically fit data from the SNANA software package, the RMS values show that the total error for m_b (Σ_1) should be 0.1020, error for x_1 (Σ_2) should be 0.4490, and error for c (Σ_3) should be 0.09086.

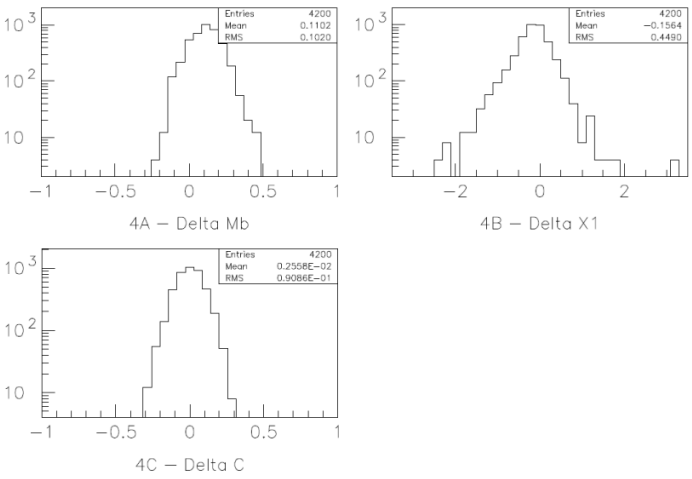

Figures 4A-4C – The above plots are all for the Monte Carlo simulated supernovae with color smearing = 0.10. Figure 4A shows the plot for Δm_b with RMS = 0.1020. Figure 4B shows the plot for Δx_1 with RMS = 0.4490. Figure 4C shows the plot for Δc with RMS = 0.09086.

Figures 4A-4C demonstrate that this method is useful in estimating the total errors based on this ad hoc model. This, however, introduces a dependence on a model whose validity is uncertain. It does allow us to use the plots in Figures 4A-4C to determine the intrinsic error matrix that must be added to the measured error from the data, by using the values for the intrinsic errors from the plots. Thus, using the SALT2mu program, we can find the correct total error that is determined from the simulations. Table 4 lists the values for the error matrices of the total error, measurement error, and our final result for the intrinsic error that must be added using the equation for σ_i^2. Similar calculations can be used to estimate the off-diagonal part of the error matrix. Based on these calculations we use the following correlations: m_b and x_1 = -0.3, m_b and c = 0.65, x_1 and c = -0.1.

TABLE 4 Errors for Type IA Supernovae

Error for Parameter:	m_b	x_1	C
Measured Error	0.0506	0.4890	0.0384
Total Error (CS Model)	0.1020	0.4490	0.0909
Total Error (SALT2mu)	0.1022	0.4821	0.0878
Intrinsic Error Needed	0.07	0.10	0.08

Table 4 – List of the values for measurement, total, and intrinsic errors for the parameters of apparent light intensity (m_b), shape (x_1) and color (c). Total error is listed as measured by the plots from the color smearing model, as well as the values used directly by the SALT2mu program.

Table 5 lists the final results of running the SALT2mu program with the newly determined intrinsic errors and the measurement errors in SALT2mu for both the standard Monte Carlo simulation as well as the real data. In both instances, the χ^2/DOF is close to but lower than 1. The fact that the χ^2/DOF is close to 1 is a significant success for the color smearing model since the amount of color smearing was determined independently of the Hubble diagram (using the photo-z fits). We were able to determine a way to estimate the intrinsic errors (listed in Table 4) in order to acquire fairly close results for α and β in the simulation, where we know the correct result. Therefore, we can see from these values that the use of this model works as one method for estimating the intrinsic error for the shape and color parameter coefficients, α and β, for use in determining the distance moduli (μ(z)).

TABLE 5 Final Results for α and β

	χ^2/DOF	α	$\Delta\alpha$	β	$\Delta\beta$
SNANA Sim.	3716/4318	0.0919	0.00236	2.562	0.0274
SDSS-II Data	219/344	0.1140	0.01377	3.394	0.1385

Table 5 – This table lists the final results of α and β with errors ($\Delta\alpha$ and $\Delta\beta$) for the SNANA simulation as well as the real SDSS-II SN Survey data taken in fall seasons of 2005, 2006, and 2007.

CONCLUSIONS

The results of this project show that dividing the data into multiple redshift bins of at least 4, makes it possible to separate the determination of the α and β parameters from the determination of the cosmology. Using an extreme amount of bins is unnecessary since it ultimately increases computation time without much statistical benefit. Using our method, we find that an intrinsic error is needed in order to determine the correct shape and color parameter coefficients, α and β respectively. When no intrinsic error is present, the χ^2/DOF estimation is much too high and does not yield statistically accurate results. Therefore, both α and β depend on the intrinsic errors in the SALT-II model, and cannot be determined from measurement error alone.

Since the 3x3 error matrix that we use in the program is symmetric, we were working with 6 unknown variables: the three intrinsic errors (Σ) and the correlation coefficients between m_b, x_1, and c with values listed previously. By applying the color smearing model to the Monte Carlo simulation with the photoz reconstruction, we determine that the simulation needs a color smearing equal to 0.10 to match the data. We can use the non-photoz simulation to then determine the distribution of the Δ values for each variable m_b, x_1, and c and use their RMS values as the total error. We then can apply this total error in the program SALT2mu to add in the required intrinsic error to the measurement error to match our calculated total error. The results of this method yield values for the intrinsic error matrix with Σ_1 = 0.07 Σ_2 = 0.10 Σ_3 = 0.08 with a final χ^2/DOF = 3716/4318 for the values of α and β.

With the known correlations between m_b and x_1, m_b and c, and x_1 and c, the results can be applied to the 3 year

SDSS-II SN Survey data. Our final results, as listed in Table 5, yield values of $\alpha = 0.0919$ and $\beta = 2.562$ for the Monte Carlo simulation with the correct values being $\alpha = 0.11$ and $\beta = 2.60$. For the SDSS-II data, our results are $\alpha = 0.1140$ and $\beta = 3.394$. As the tables indicate, these results show that our simulation is roughly consistent with data, and this serves as one general method for determining the shape and color parameter coefficients. However, looking at the final values by running the program with our estimated intrinsic error values implies that we are entering a value that is too low for the color parameter coefficient β.

ACKNOWLEDGEMENTS

I would also like to acknowledge and thank the Wayne State University Research Experience for Undergraduates program for this research opportunity and Scott Dodelson for his advice and discussion on the topic of maximum likelihood approximation with fitting data to lines with errors in x and y (Appendix).

REFERENCES

Gunn, J. E. et al. 1998 AJ, 116, 3040
Gunn, J. E. et al. 2006, AJ, 131, 2332
Guy, J. et al. 2007, A&A, 466, 11
Frieman, J. A. et al. 2008, AJ, 135, 338
Fukugita, M. et al. 1996, AJ, 111, 1748
Hayden, B. et al. 2010, ApJS, published (arXiv:astro-ph/1001.3428)
Ivezi´c, ˇZ. et al. 2004, Astronomische Nachrichten, 325, 583
Kessler, R. et al. 2009a, ApJS, accepted for publication (arXiv:astro-ph/0908.4274)
Kessler, R. et al. 2009b, PASP, accepted for publication (arXiv:astrop-ph/0908.4280)
Kessler, R. et al. 2009c, ApJ, accepted for publication (arXiv:astro-ph/1001.0738v2)
Lupton, R. et al. 2001, in ASP Conf. Ser. 238: Astronomical Data Analysis Software and Systems X, ed. F. R. Harnden, Jr., F. A. Primini, & H. E. Payne, 269-+
Press, W. H. et. al. 1988, Numerical Recipes in C, (Cambridge University Press, New York, NY)
Sako, M. et al. 2008, AJ, 135, 348

APPENDIX: MATHEMATICAL EXERCISES TO IMPROVE SALT2mu

TEST 1 – Elementary χ^2 Minimization (Ignoring Errors in X) vs. Fitting with Errors in X and Y

The most elementary method used for estimating the slope of a set of correlated data points, and the method used in our data analysis assumes error only in one variable. Our initial method minimizes a χ^2 in order to find the correct slope of the data using the method given in Press, et. al. (1988). We take a look at methods of better estimating the slope (s) through a simulation of data points distributed about a straight line y=sx, and by minimizing the χ^2 value between the data points and the estimated straight line. We use the pseudo-random number generator embedded in the C compiler to generate 10,000 data points with true slope value s = 2.5 using a Gaussian distribution for the errors in x and y as shown in Figure 5. Generally, the data we work with is analyzed by the equation:

$$M_b = m_b - \mu(z) + \alpha x_1 + \beta c. \quad (7)$$

However, in order to explore this mathematical model and a different method of maximum likelihood estimation, we use the simplified y=sx for only two variables y and x. To relate it back to the original, it could be looked at as $M_b = \alpha x_1$ where we are looking to find α with parameters M_b and x_1.

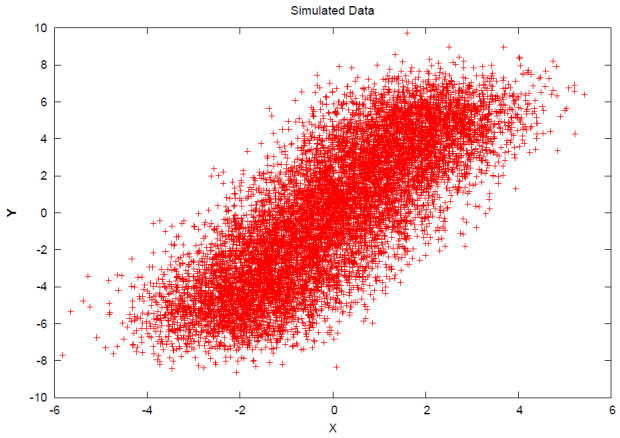

Figure 5 – The simulated data set of 10,000 points used in the exercise to compare the two fitting methods, plotted as x vs. y with a Gaussian distribution in the errors for x and y.

We then calculate the χ^2 for the data set by incrementing the slope at an assigned value of 0.05 from 0.00 to 5.00 and finding the corresponding slope with the smallest $\chi^2 = \sum_i^N \frac{(y_i - sx_i)^2}{\sigma_y^2 + s\sigma_x^2}$ for i being each simulated data point. We can compare the estimated slope value found by minimizing this χ^2 output, to the new method ($\chi^{2'}$).

The new method for estimating the slope proposed by Scott Dodelson (private communication) was added to the same program and applied to the same data set. The expression for $\chi^{2'}$ is obtained by integrating analytically over all possible x and y to find the likelihood (P(x,y)) of getting each x and y value with error σ_x and σ_y:

$$P(x^{meas}, y^{meas}|s) =$$

$$\frac{1}{\sigma_x \sigma_y} \int_{x_{min}}^{x_{max}} dx \int dy e^{-\frac{(x-x^{meas})^2}{2\sigma_x^2}} e^{-\frac{(y-y^{meas})^2}{2\sigma_y^2}} \delta(y - sx). \quad (8)$$

The complete solution after derivation is then:

$$\chi^{2'} \equiv \sum_i^N \frac{(y_i - sx_i)^2}{\sigma_y^2 + s\sigma_x^2} - 2\ln\left[\theta(x_0 - x_{min})P\left(\frac{1}{2}, A(x_0 - x_{min})^2\right) + \theta(x_{max} - x_0)P\left(\frac{1}{2}, A(x_0 - x_{max})^2\right)\right], \quad (9)$$

where P(a,b) is the incomplete gamma function,

$$A = \frac{\sigma_y^2 + s^2\sigma_x^2}{2\sigma_x^2\sigma_y^2}, \quad (10)$$

$$x_0 = \frac{\sigma_y^2 x^{meas} + s y^{meas}\sigma_x^2}{\sigma_y^2 + s^2\sigma_x^2}, \text{ and} \quad (11)$$

$$\theta = 1 \; for \; x > 0 \; and \; -1 \; for \; x < 0. \quad (12)$$

The program uses the simulated data to calculate both χ^2 and $\chi^{2'}$ for increasing slopes from 0.00 to 5.00 as before, but now prints out the standard and new methods side by side. The program can also be used to calculate the χ^2 and $\chi^{2'}$ values by running through possible slope values 's' at much smaller intervals (0.0001), as was done in some of the results below, in order to more precisely estimate the value of 's'. The results from the new $\chi^{2'}$ estimator are found for the correct values of the interval x_{min}=-2.5 to x_{max}=2.5 as well as the slightly wrong intervals of x_{min}=-2.0 to x_{max}=2.0 and x_{min}=-3.0 to x_{max}=3.0. Since the original estimator does not use these values, the outcome of the standard method is the same in each following situation but is used as a comparison.

RESULTS

Upon first running the two estimators with x_{min}=-2.5 x_{max}=2.5 for the new method (Figures 6&7), the results seem to indicate that both the standard method and the new $\chi^{2'}$ are able to correctly estimate the value of the slope at 2.5 (Figure 6) As mentioned previously, the program was then run with slope values of smaller interval 0.0001 in order to better estimate the value of the slope (s) and to look at the error as shown by both straight line fits (Figure 7). The standard χ^2 minimization estimated the slope to be 2.4920 for all values of x_{min} and x_{max}, since it does not use these values in the calculations. The new $\chi^{2'}$ method estimated the slope to be 2.5160. We can see that the standard method is off from the true value by 0.0080, while the new method is off by 0.0160. However, the plots of the χ^2 and $\chi^{2'}$ data would indicate that the error for the new method is actually less than that of the standard estimator. Figure 6 shows the results of the two estimations when the

range in x is -2.5<x<2.5. Both curves are compatible with the correct value for s=2.5. Figure 7 shows the regions around the minimum more precisely, indicating that the increase in χ^2 at the correct slope is less than 1 for the first method and only slightly larger than 1 for $\chi^{2'}$.

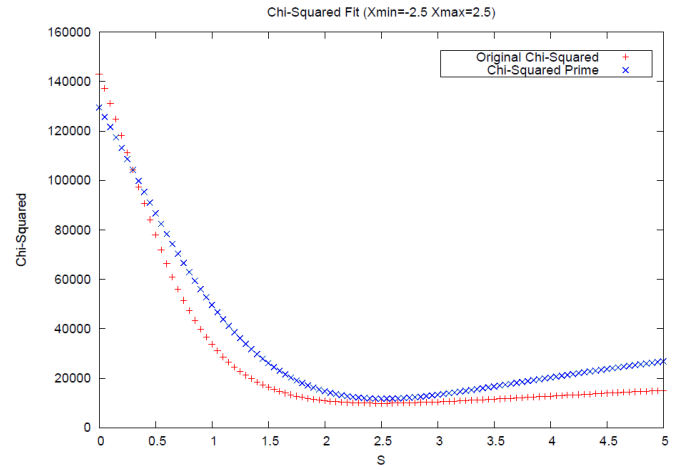

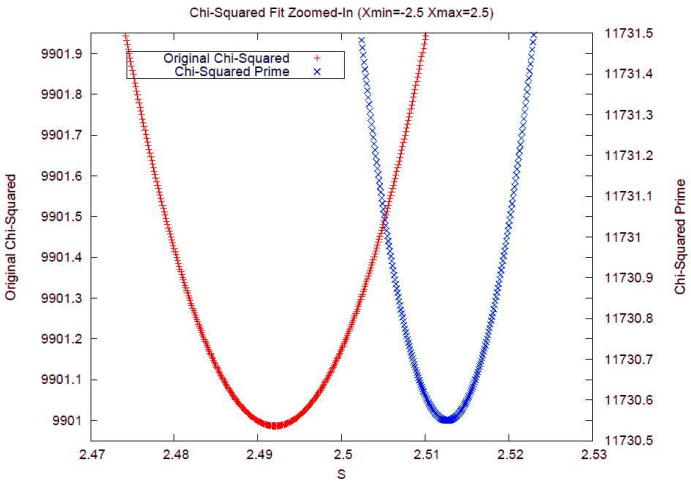

Figures 6 & 7 – Figure 6 is a plot of slope (s) vs. the χ^2 results for χ^2 and $\chi^{2'}$ methods for x_{min}= -2.5 and x_{max}= 2.5. Figure 7 shows the same results with a smaller range to see the results more accurately with χ^2 on the y1 axis and $\chi^{2'}$ on the y2 axis.

We test the method in the same manner, but change the x_{min} and x_{max} values to test the results for situations when the correct distribution in the x values in unknown. We use the values of x_{min} = -2.0, x_{max} = 2.0, and x_{min} = -3.0, x_{max} = 3.0. Figure 8 shows the results when the range in x is decreased to less than the correct distributed range (-2.0 to 2.0). The results for χ^2 do not change since these values do not play a role in the equations for that method. However, figure 9 indicates that $\chi^{2'}$ is now off by 0.3059 on the positive end, and the result is therefore clearly biased.

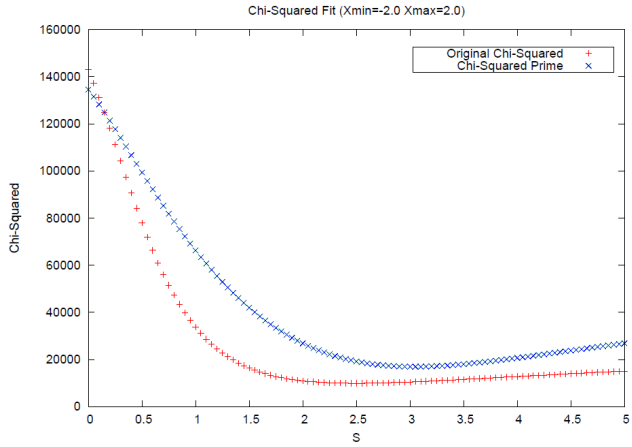

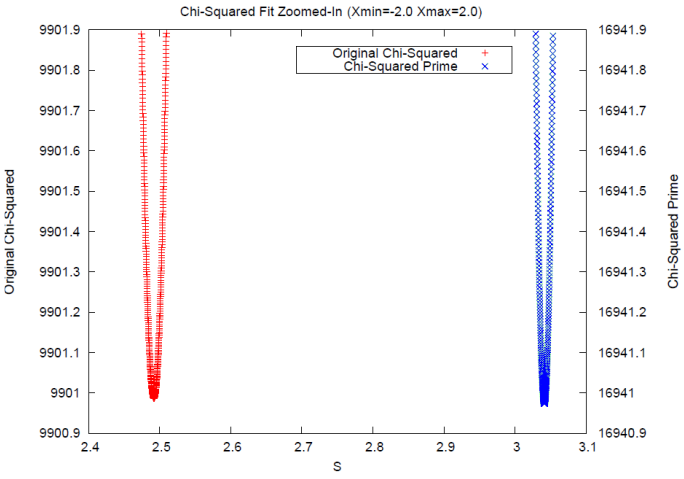

Figures 8 & 9 – Figure 8 is a plot of slope (s) vs. the χ^2 results for χ^2 and $\chi^{2'}$ methods for x_{min} = -2.0 and x_{max} = 2.0. Figure 9 shows the same results with a smaller range to see the results more accurately with χ^2 on the y1 axis and $\chi^{2'}$ on the y2 axis.

In the final test, with x_{min} = -3.0 and x_{max} = 3.0, the results are shown in Figures 10 and 11. As these two figures indicate, just as when the estimated range is decreased, when the estimated range for x is increased, the results are off by a larger number, and in this case by 0.5413.

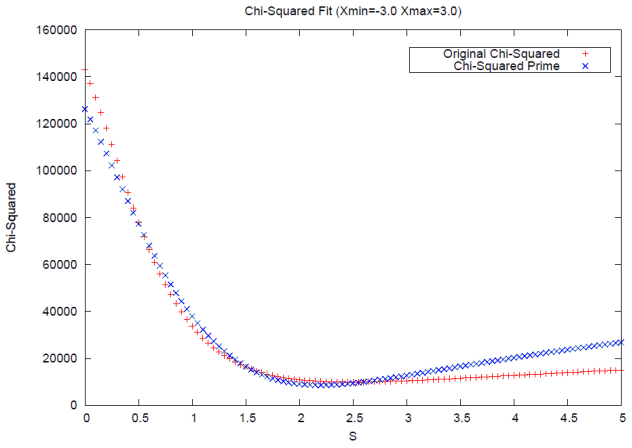

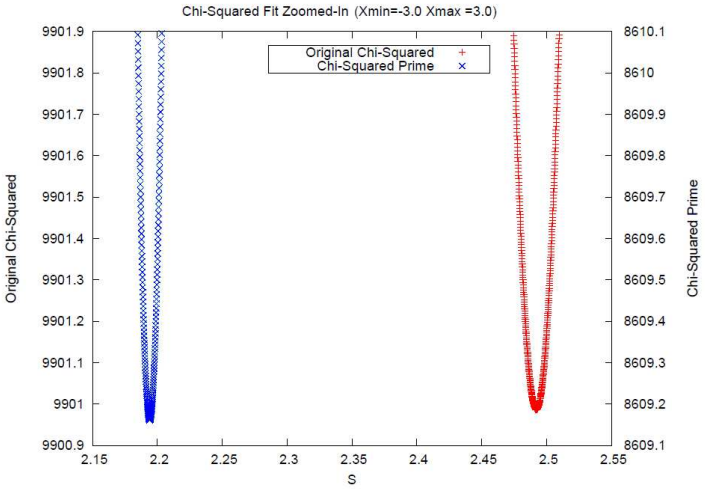

Figures 10 & 11 – Figure 10 is a plot of slope (s) vs. the χ^2 results for χ^2 and $\chi^{2'}$ methods for x_{min} = -3.0 and x_{max} = 3.0. Figure 11 shows the same results with a smaller range to see the results more accurately with χ^2 on the y1 axis and $\chi^{2'}$ on the y2 axis.

These results indicate that when the assumed values of x_{min} and x_{max} are limited to a smaller range than the full simulated data set, the slope (s) that is estimated by the $\chi^{2'}$method is higher than the true value of s, which is given in this particular simulation to be 2.5. In the other case, when x_{min} and x_{max} are outside of the simulated data's range, the slope is estimated by the program to be lower than the true value.

The overall results seem to show that when the new $\chi^{2'}$ estimator is given a correct range for x, defined by x_{min} and x_{max}, it is able to calculate the correct value of the slope (s) with minimal error, very close to the results shown from the standard χ^2 minimization. However, when the values of x_{min} and x_{max} are unknown and are off from the real values, the new method's slope (s) estimate is not as reliable as the standard method. Thus, if the statistical range of a given set of measured data is known, the correlation is found with better error, than with the initial method.

TEST 2 – CALCULATING TWO PARAMETERS SIMULTANEOUSLY

The final thing we wanted see is if we would be able to calculate several parameters simultaneously in regards to the slope equation, namely a parameter and the error associated with y. Therefore, for this exercise ($\chi^{2''}$) we changed the program and the initial error values in x and y to σ_x = 0.0 and σ_y = 0.75. The likelihood equation for this scenario becomes:

$$L(x,y) = \prod_{i=1}^{N} \frac{1}{\sqrt{2\pi}\sigma_y} e^{\frac{-(y_i - sx_i)^2}{2\sigma_y^2}}. \qquad (13)$$

When you take the natural log of both sides of this equation, the following equation can be used by incrementing both slope (s) and the error (σ_y) to determine the minimum χ^2:

$$-2\ln L = \sum ln\sigma_y^2 + \frac{(y_i - sx_i)^2}{\sigma_y^2} + C. \qquad (14)$$

RESULTS

The two plots in Figures 12 and 13 show from different views that the results of the $\chi^{2''}$ estimation was able to correctly determine both the slope of the data set s=2.5 and the correct σ_y = 0.75.

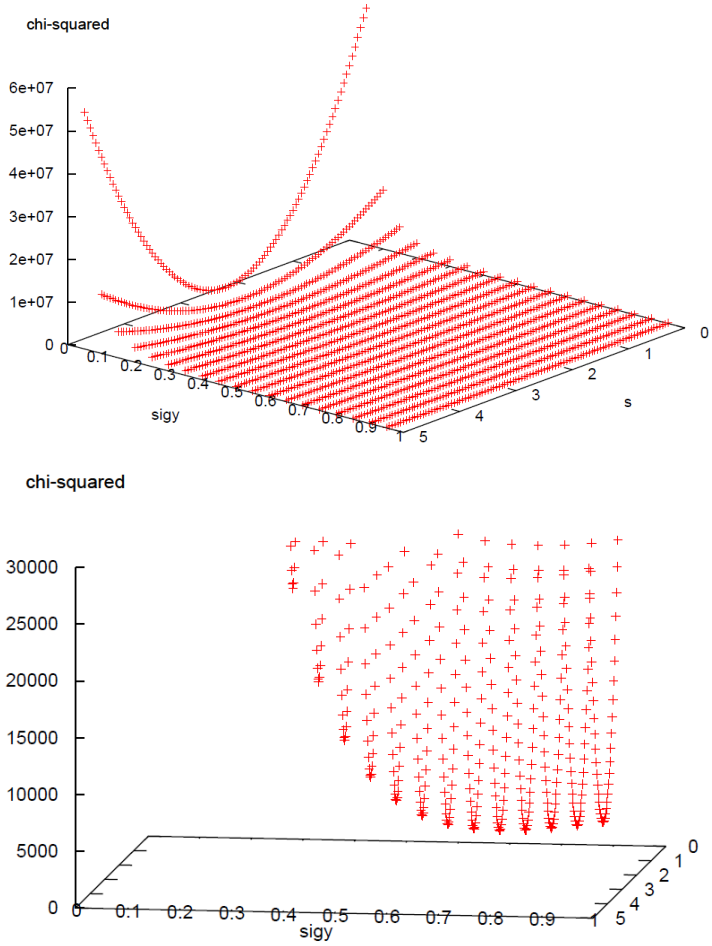

Figures 12 & 13 – Figure 12 shows a 3 dimensional plot of s and σ_y against the χ^2 calculations for the $\chi^{2''}$ method and shows that the minimum is at a value of s = 2.5. Figure 13 is the same plot, but with a small range to indicate that the minimum is also at σ_y = 0.75.

Anharmonic Oscillator Potentials:

Exact and Perturbation Results

Benjamin T. Floyd, Amanda M. Ludes, Chia Moua, Allan A. Ostle, and Oren B. Varkony

Department of Physics,

University of Nebraska at Omaha,

Omaha, Nebraska 68182

(Submitted for publication at the Journal of Undergraduate Research in Physics)

(November 28, 2011)

Abstract

In order to determine the first four energy levels of our anharmonic potential, we will compute the first four eigenvalues of the anharmonic oscillator potential with a quartic term using Heun polynomials and Maple software packages. We will then compare them to the results obtained from the conventional perturbation method, treating the quartic term as perturbation up to the third order. Through this it can be shown that generally the two methods agree well with each other when the perturbing potential is weak. Nevertheless, the perturbation results will start to deviate from those of the exact solutions at stronger perturbation potentials and higher excited states.

I. Introduction

When learning the time-independent perturbation method of quantum mechanics, most students are taught that as long as the perturbation potential is not strong, the corrections in eigenvalues and eigenfunctions can be calculated systematically order by order. The statement is intuitively reasonable, yet not complete. We learned from the seminal paper of Bender and Wu [1] that it was proved that the perturbation series for the ground state energy of the anharmonic oscillator with only the quartic term diverges for any non-zero coupling constant. A simple way to explain it is in the following Schrödinger equation:

$$\left[-\frac{\hbar^2}{2m}\frac{d^2}{dx^2}+\frac{1}{2}\omega^2 x^2+\alpha x^4\right]\psi = E\psi . \qquad (1)$$

That is, even though α, the coupling constant of the quartic term, can be very small, after large enough values of x the quartic potential αx^4 eventually supersedes the harmonic potential $m\omega x^2/2$, and it can no longer be considered weak. Therefore during practical computation, for the perturbation scheme to be applicable not only do we have to be certain that the coupling constant is small enough, but we also have to examine the region of validity. However, when the method is taught in most commonly adopted textbooks, major efforts are spent on deriving the general formulas of energy and wave function corrections and applying them to a few well known examples as mentioned above, but no demonstrations are provided. In all likelihood, the inability to solve Eq. (1) analytically is one of the reasons. By now, we have learned that Schrödinger equations like Eq. (1) can be solved in terms of Heun polynomials that are explained thoroughly in the references [2] mentioned in Maple Help pages. Computer algebra software packages in Maple 14 are capable of evaluating these special functions, rendering the exact solution attainable.

In this work, we will calculate the total energies of the first four eigenvalues of the anharmonic oscillator with only the quartic term, using both the perturbation and numerical methods. First we shall summarize the procedures in deriving the leading three orders of energy

corrections and apply them to the quartic potential, and then we will highlight the numerical schemes in computing the ground and first three excited state energies of the anharmonic oscillator potentials. Finally we will compare results obtained from these two methods and discuss the applicability of the perturbation method.

II. Theory

Before starting the perturbation and numerical calculations, we reduce the Schrödinger equation, Eq. (1), into a dimensionless differential equation: first we substitute $x = \beta z$, where β is an undetermined parameter, and divide the whole Eq. (1) by $\frac{\hbar^2}{2m\beta^2}$. We notice, then, that as we set $\beta = \sqrt{\frac{\hbar}{m\omega}}$, $\gamma = \frac{2\alpha\hbar}{m^2\omega^3}$ and $\varepsilon = \frac{2E}{\hbar\omega}$, a new differential equation emerges,

$$\left[-\frac{d^2}{dz^2} + z^2 + \gamma z^4\right]\psi = \varepsilon\psi . \qquad (2)$$

From there on, it is clear that only the parameter γ in this problem controls the strength of the perturbation potential.

It is well known that besides the simple harmonic oscillator and hydrogen atom, most of the time-independent Schrödinger equations cannot be solved analytically. For many practical cases, we solve the problems by applying the perturbation method mentioned in Griffiths' quantum mechanics textbook [3]. That is, we split the Hamiltonian $\hat{H}$ into two parts: one is the unperturbed Hamiltonian H^0, for which we know all the associated eigenvalues $E_n^{(0)}$ and eigenstates $\psi_n^{(0)}$, and the additional term H', usually referred to as perturbation,

$$\hat{H} = H^0 + \lambda H'. \qquad (3)$$

Here λ is a coupling constant which is commonly used to keep track the strength of perturbation H' and is ideally a small number. Later, however, it was turned to 1, so it only serves as an

indicator while deriving the energy corrections. Then we assume the eigenvalues E_n and eigenstates ψ_n of $\hat{H}$ can be expressed as power series in λ:

$$E_n = E_n^{(0)} + \lambda E_n^{(1)} + \lambda^2 E_n^{(2)} + \lambda^3 E_n^{(3)} + \ldots.$$

$$\text{and} \qquad \psi_n = \psi_n^{(0)} + \lambda \psi_n^{(1)} + \lambda^2 \psi_n^{(2)} + \lambda^3 \psi_n^{(3)} + \ldots. \qquad (4)$$

where $E_n^{(1)}$, $E_n^{(2)}$ and $E_n^{(3)}$ are the first, second and third order correction to the eigenvalues respectively, and $\psi_n^{(1)}$, $\psi_n^{(2)}$ and $\psi_n^{(3)}$ are the first, second and third order correction to the eigenfunctions, respectively. After we substitute Eq. (2) into the Schrödinger equation, sort out terms in the order of λ and make use of the orthogonality and completeness properties of the eigenfunctions of $\hat{H}$, the lower order corrections of eigenvalues and eigenfunctions are derived as in standard quantum mechanics textbooks [3]. In simple notation, we only present the energy corrections: first let

$$V_{mn} = \left\langle \psi_m^{(0)} \middle| H' \middle| \psi_n^{(0)} \right\rangle \text{ and } \qquad \Delta_{mn} = E_m^{(0)} - E_n^{(0)}, \qquad (5) \qquad \text{then we have}$$

$$E_n^{(1)} = V_{nn}, \qquad E_n^{(2)} = \sum_{m \neq n} \frac{|V_{nm}|^2}{\Delta_{nm}}, \qquad \text{and} \qquad E_n^{(3)} = \sum_{l,m \neq n} \frac{V_{nl} V_{lm} V_{ml}}{\Delta_{nl} \Delta_{nm}} - V_{nn} \sum_{m \neq n} \frac{|V_{nm}|^2}{\Delta_{nm}^2}. \quad (6)$$

In this work we only go up to the third order correction; of course, it is possible to pursue higher orders by following the procedures cited in the quantum mechanics textbook [3]. Generally in the summations of Eq. (4) we should include all the non-zero matrix elements. Fortunately the simple harmonic oscillator is our unperturbed Hamiltonian H^0, and the perturbation potential we considered is quartic, so there are only a few non-vanishing terms due to the raising and lowering ladder operators constructed from the original eigenstates. This is presented in Chapter 2 of the quantum mechanics textbook [4], and energy corrections can be computed accordingly.

In fact, the analytical solutions of the Schrödinger equation, Eq. (2), can be expressed in terms of the linear combination of two linearly independent Heun Triconfluent equations HeunT_1 and HeunT_2 [2], abbreviated as H_1 and H_2. Both of these are complex functions of the scaled

variable z, parameter γ, and eigenvalue ε. They have different asymptotic behaviors. One may reach zero when $z \to \infty$ and diverge as $z \to -\infty$, and the other one is exactly the opposite:

$$\psi(z,\gamma,\varepsilon) = C_1 H_1(z,\gamma,\varepsilon) + C_2 H_2(z,\gamma,\varepsilon) \tag{7}$$

where C_1 and C_2 are two arbitrary constants to be determined from the asymptotic conditions. Since we are looking for bound state solutions—that is, the wave functions have to vanish as z approaches to both positive and negative infinities—

$$\psi(z,\gamma,\varepsilon) \to 0 \text{ when } z \to \pm\infty . \tag{8}$$

To facilitate numerical calculations, we require that the wave functions vanish at a finite range $\pm R$ to approximate the asymptotic behavior of wave functions at positive and negative infinity. Actually, we observe that the first few excited state wave functions of simple harmonic oscillators approach zero around R= 4 to 5. Thus we first assume R=4.5, with given γ, and we numerically compute ε by solving the following 2x2 determinant equation which is only a function of ε,

$$\begin{vmatrix} H_1(R,\gamma,\varepsilon) & H_2(R,\gamma,\varepsilon) \\ H_1(-R,\gamma,\varepsilon) & H_2(-R,\gamma,\varepsilon) \end{vmatrix} = 0 \tag{9}$$

It turns out both the HeunT_1 and HeunT_2 are complex and often huge, hence they require quite a lot of digits—roughly 30 to 70 depending on different asymptotic conditions—and computation time to reach convergence. Yet when reaching the zeroes of the determinant, Eq. (7) is purely real and we find that the roots correspond to the eigenvalues of Eq. (2). In this work, we only compute the first four eigenvalues and use them to plot the wave functions. Results with various γ, such as energies obtained from both the numerical and perturbation methods and wave functions computed from Heun polynomials, can be seen in the Section III. Finally, we select R carefully: first we set R= 4.5, then gradually increase it to 6 and notice the values of the roots change minutely. We declare that R ~ 5 is effectively equivalent to infinity. Afterward, we plot the wave functions and observe that indeed all the wave functions vanish before R = 5.

III. Results and discussion

Based on Equations (5) and (6), we calculate the first four perturbed total energies of the anharmonic oscillator, ε_0 to ε_3, up to the third order γ^3,

$$\varepsilon_0 = 1 + \frac{3}{4}\gamma - \frac{21}{16}\gamma^2 + \frac{333}{64}\gamma^3$$

$$\varepsilon_1 = 3 + \frac{15}{4}\gamma - \frac{165}{16}\gamma^2 + \frac{3915}{64}\gamma^3$$

$$\varepsilon_2 = 5 + \frac{39}{4}\gamma - \frac{615}{16}\gamma^2 + \frac{20079}{64}\gamma^3$$

$$\varepsilon_3 = 7 + \frac{75}{4}\gamma - \frac{1575}{16}\gamma^2 + \frac{66825}{64}\gamma^3 \qquad (10)$$

Just by inspecting the increasing coefficients, we realize that in order to have reasonable perturbed energies, the values of γ have to be very small.

In Table 1 and Figure 1, we present the comparison of results obtained from numerical and perturbation methods.

	γ	Numerical	2nd Order Perturbation	Percent Difference (2nd Order)	3rd Order Perturbation	Percent Difference (3rd Order)
n = 0	0.05	1.03473	1.03422	0.0494%	1.03487	-0.0134%
	0.075	1.05043	1.04887	0.1488%	1.05106	-0.0602%
	0.1	1.06529	1.06188	0.3206%	1.06708	-0.1679%
n = 1	0.05	3.16723	3.16172	0.1740%	3.16937	-0.0674%
	0.075	3.23967	3.22324	0.5071%	3.24905	-0.2895%
	0.1	3.30687	3.27186	1.0583%	3.33305	-0.7916%
n = 2	0.05	5.41726	5.39141	0.4772%	5.39141	0.4772%
	0.075	5.59031	5.51504	1.3464%	5.51504	1.3465%
	0.1	5.74796	5.59063	2.7371%	5.59063	2.7372%
n = 3	0.05	7.77027	7.69141	1.0149%	7.82192	-0.6648%
	0.075	8.07718	7.85254	2.7812%	8.29304	-2.6724%
	0.1	8.35268	7.89063	5.5318%	8.93477	-6.9688%

Table 1. Comparison of the first four eigeneneriges calculated from numerical and perturbation methods, both second and third order.

We further notice two general features in perturbation results up to second order: first, the agreements are far better at the low-lying states than those of the higher excited states. The percentage discrepancies in n=0 and 1 are less than 1%, and those of n=2 and 3 are greater than 1%. Second, when γ=0.05, the percentage discrepancies for all the first four states are small and not greater than 1% except n=3. As γ increases to 0.075 and 0.1, most of the percentage discrepancies exceed 1%; particularly, the third excited state (n=3) reaches 5.5%.

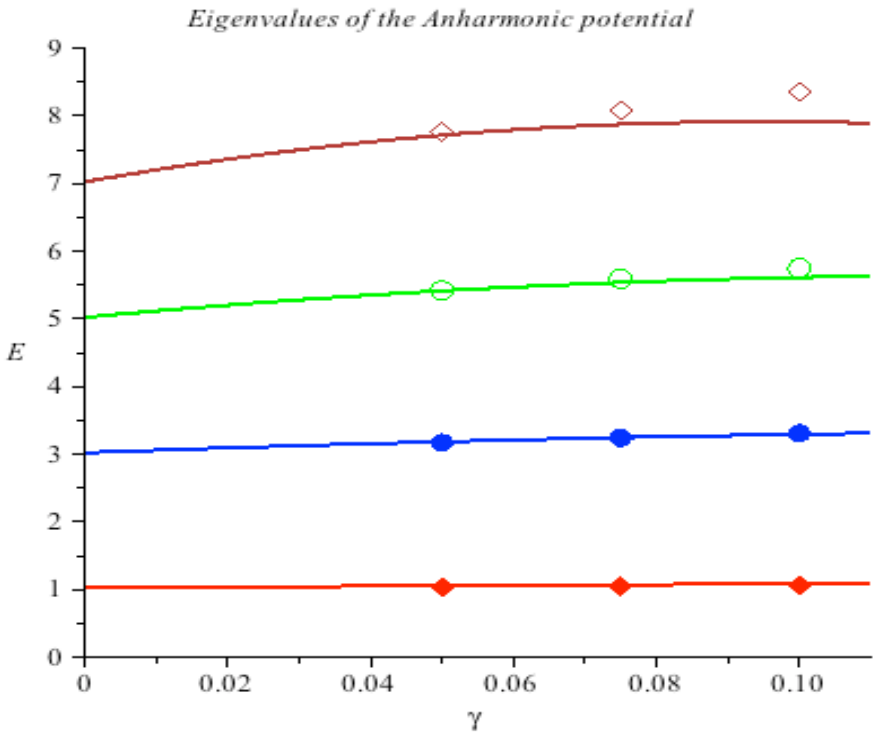

Figure 1. Comparison of the first four eigeneneriges calculated from numerical (discrete symbols) and second order perturbation methods (continuous curves). Ground state (red), first (blue), second (green) and third (brown) excited states.

We can interpret these features from observing the wave functions displayed in Figure 2: notice that the wave functions of the ground state (red) and first excited state (blue) vanish as z~3, whereas those of the second (green) and third (brown) excited states drop to zero when z at least exceeds z~3.5. This is a crucial change, since we can easily deduce that the quartic potential z^4 surpasses harmonic potential z^2 at the crossover range z_c~3.16, where $z_c=1/\sqrt{\gamma}$, when γ=0.1.

This implies the basis that the perturbation method is valid when the perturbation is relatively weak or less than 10%. To further clarify our claim, we carry out the same analysis by including the third order correction: similarly in Table 1, we find that the improvements on the low-lying states, n=0 and 1, are small and incremental, yet overshoot the exact values. The third order results are larger than the exact values, whereas those of the second order are less.

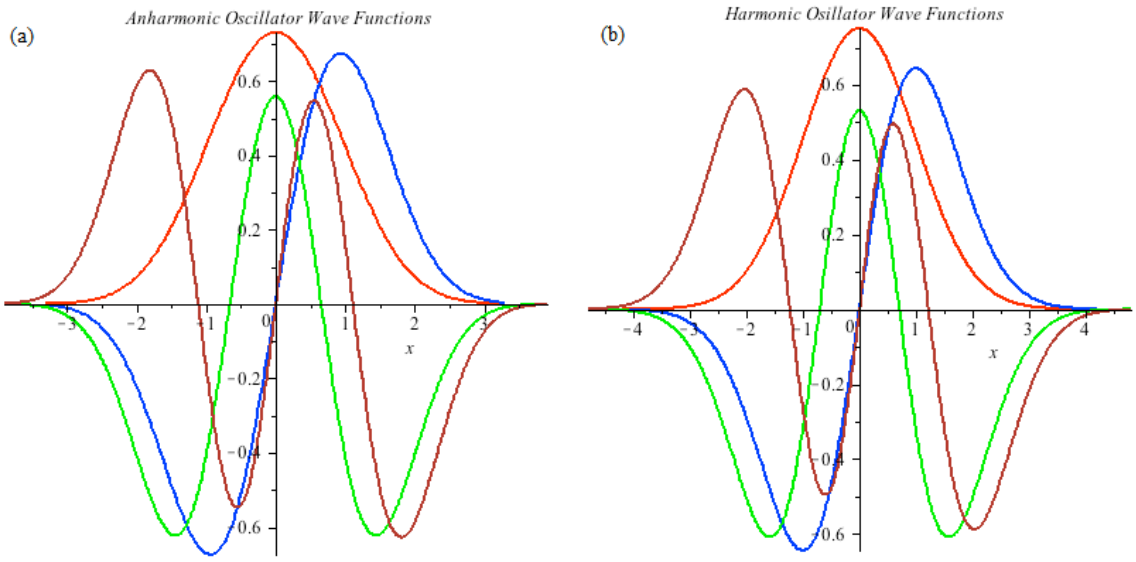

Figure 2. (a) Wave functions of the first four eigenstates of the anharmonic potential with $\gamma = 0.1$: ground state (red), first (blue), second (green) and third (brown) excited states. (b) First four eigenstate wave functions of the harmonic oscillator are used for comparison. Apparently wave functions in (a) and (b) are similar, but notice that the ranges of (b) are longer.

This effect is more prominent for higher excited states like n=2 and 3: the percentage discrepancies change from 2.74 and 5.5% in second order correction results to -2.72 and -7.0% for n=2 and 3 respectively, in third order correction results, as shown in Table 1 and Figure 3.

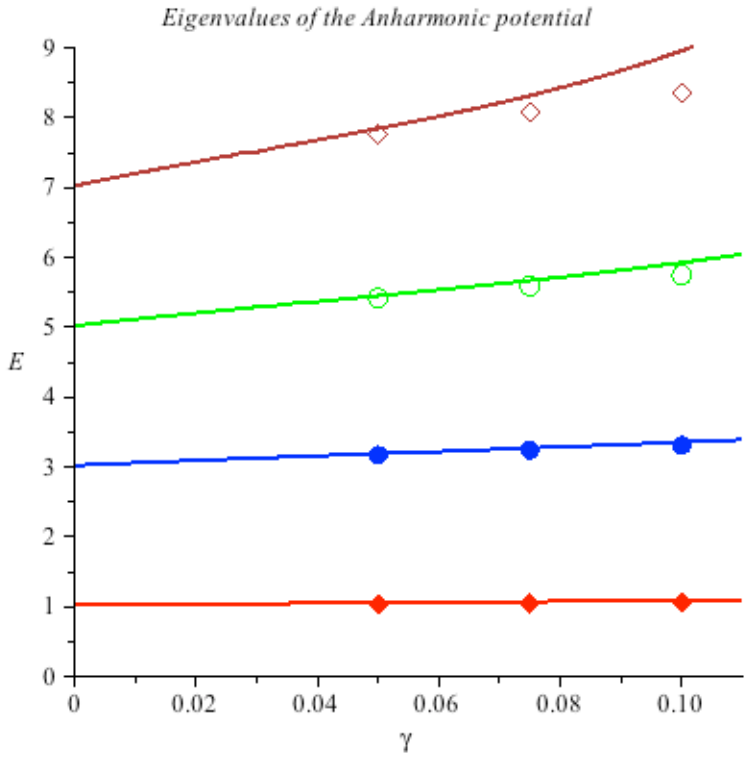

Figure 3. Comparison of the first four eigeneneriges calculated from numerical (discrete symbols) and third order perturbation methods (continuous curves). Ground state (red), first (blue), second (green) and third (brown) excited states.

In other words, adding more correction terms may lead to oscillatory behavior in total perturbed energies. Nevertheless, in order to verify this assertion it is necessary to have higher-order calculations, which as mentioned in the quantum mechanics textbook [3], is a lengthy calculation. Hopefully this calculation will be carried out in the future.

Finally, like the previous works [5, 6] published at the Journal of Undergraduate Research in Physics by physics majors from the University of Nebraska at Omaha, we have intensively used Maple packages to perform all the analytical and numerical calculations. We find the packages are efficient and helpful in our work. Our worksheets are available for interested readers. Please send requests to the attached addresses.

IV. Conclusion

In summary, we calculated the first four eigenenergies of the harmonic oscillator potential with the quartic term using numerical and conventional perturbation methods. We found that the two methods agree well with each other when the perturbing potential is weak and particularly at the low-lying states. As the perturbing potential gets stronger, particularly at the higher excited states, we noticed the perturbation results start to deviate from those obtained from the numerical schemes. We elucidated this behavior by comparing the strengths of harmonic and quartic potentials and uncovered that the conventional perturbation method starts to be ineffective when the wave functions exceed the crossover range.

V. Acknowledgements

We are grateful to the University of Nebraska at Omaha (UNO) Physics Department for providing us with an excellent atmosphere for study. We would also like to express our appreciation to Professors Wai-Ning Mei, Daniel Wilkins, and Renat Sabirianov of the Physics Department for their constant guidance and support to the UNO Society of Physics Students.

VI. References

1. C. M. Bender and T. T. Wu, Phys. Rev., 184, 1231-1260, (1969).

2. A. Decarreau, M. C. Dumont-Lepage, P. Maroni, A. Robert, and A. Ronveaux, "Formes Canoniques de Equations confluentes de l'equation de Heun." Annales de la Societe Scientifique de Bruxelles, Vol. I-II. (1978): 53-78. A. Ronveaux, ed. “Heun's Differential Equations”. Oxford, England: Oxford University Press, (1995). S. Y. Slavyanov and W. Lay, “Special Functions, A Unified Theory Based on Singularities”. Oxford, England: Oxford Mathematical Monographs, (2000).

3. D. J. Griffiths, “Introduction to Quantum Mechanics” (Upper Saddle River, NJ, Pearson Preston Hall, 2005, second edition) Chapter 6, and the references cited therein, especially Footnote 5 on P. 256.

4. *ibid,* Chapter 2, Section 2.3.

5. J. Koch, C. Schuck, and B. Wacker, "Excited states of the anharmonic oscillator problems: variational method", Journal of Undergraduate Research in Physics 21, (2008). http://www.jurp.org/

6. E. R. Hedgahl, T. L. Johnson III, S. E. Schnell, and A. R. Ward, "Systematic convergence in applying the variational method to the anharmonic oscillator potentials”, Journal of Undergraduate Research in Physics 21, (2008). http://www.jurp.org/